Research Article

Muhammad Hasnain Jameel*, Aqeela Yasin, Samia, Mohd Zul Hilmi Bin Mayzan*, Muhammad Sufi bin Roslan, Fahmiruddin Bin Esa, Mohd Arif Bin Agam, Mohd Hafiz Mohd Zaid, Khaled Althubeiti, and Mohammed Aljohani

A comprehensive study of laser irradiated hydrothermally synthesized 2D layered heterostructure $V_2O_{5(1-x)}MoS_{2(x)}$ (X = 1–5%) nanocomposites for photocatalytic application

https://doi.org/10.1515/ntrev-2024-0078
received January 31, 2024; accepted July 16, 2024

Abstract: It has been studied that both two-dimensional (2D) MoS_2 and V_2O_5, which are classified as transition metal dichalcogenides and transition metal oxides, are good photocatalyst materials. For this purpose, the hydrothermal method was practiced to synthesize $V_2O_{5(1-x)}MoS_{2(x)}$ (X = 1–5% w/w) nanocomposites with different 1–5% w/w weight percent of MoS_2 as a prominent photocatalyst under laser irradiation for 2, 4, 6, 8, and 10 min to tune photocatalytic degradation of industrial wastage water. The surface of the 2D molybdenum nanolayered matrix was efficaciously decorated with V_2O_5 nanoparticles. The crystal phase and layered structures of the $V_2O_{5(1-x)}MoS_{2(x)}$ (X = 1–5% w/w) nanocomposites samples were verified by X-ray diffraction and scanning electron microscopy, atomic force microscopy, X-ray photoelectron spectroscopy respectively. In the range of the UV visible spectrum, the increment in light absorption from 3.6 to 14.5 $\Omega^{-1}\,cm^{-1}$ with an increase of active surface from 108 to 169 μm^2 with increased MoS_2 doping percentage. Furthermore, dielectric findings like the complex dielectric function, tangent loss, electrical conductivity, quality factors, and impedance of $V_2O_{5(1-x)}MoS_{2(x)}$ (X = 1–5% w/w) nanocomposites are studied. According to photoluminescence studies, the intensity of peaks decreases when laser irradiation time and doping percentages of MoS_2 are increased. As a result, a small peak indicates a decrement rate of electron–hole pair recombination, which increases the capacity for separation. Thermo-gravimetric analysis and differential thermal analysis results revealed that weight loss decreased from 0.69 to 0.35 mg and thermal stability increased with increased doping concentrations. Methylene blue was degraded in 150 min, proving that the prepared MoS_2-doped V_2O_5 material was a stable and economically low-cost nanocomposite for photocatalytic activity.

Keywords: laser irradiation, MoS_2-doped V_2O_5 nanocomposites, 2D heterostructure, photocatalytic applications

*** Corresponding author: Muhammad Hasnain Jameel,** Department of Physics and Chemistry, Faculty of Applied Sciences and Technology (FAST), Universiti Tun Hussein Onn Malaysia, 84600, Muar, Johor, Malaysia; Ceramic and Amorphous Group (CerAm), Faculty of Applied Sciences and Technology, Pagoh Higher Education Hub, Universiti Tun Hussein Onn Malaysia, 84600, Panchor, Johor, Malaysia, e-mail: mhasnainjamil@gmail.com
*** Corresponding author: Mohd Zul Hilmi Bin Mayzan,** Department of Physics and Chemistry, Faculty of Applied Sciences and Technology (FAST), Universiti Tun Hussein Onn Malaysia, 84600, Muar, Johor, Malaysia; Ceramic and Amorphous Group (CerAm), Faculty of Applied Sciences and Technology, Pagoh Higher Education Hub, Universiti Tun Hussein Onn Malaysia, 84600, Panchor, Johor, Malaysia, e-mail: zulhilmi@uthm.edu.my
Aqeela Yasin: School of Materials Science and Engineering, and Henan Key Laboratory of Advanced Magnesium Alloy and Key Laboratory of Materials Processing and Mold Technology (Ministry of Education), Zhengzhou University, Zhengzhou, China
Samia: Tianjin Key Laboratory of Low Dimensional Materials Physics and Preparing Technology, School of Science, Tianjin University, Tianjin, 300072, China
Muhammad Sufi bin Roslan: Department of Science and Mathematics, Center for Diploma Studies (CeDS), Universiti Tun Hussein Onn Malaysia, 84600, Muar, Johor, Malaysia
Fahmiruddin Bin Esa, Mohd Arif Bin Agam: Department of Physics and Chemistry, Faculty of Applied Sciences and Technology (FAST), Universiti Tun Hussein Onn Malaysia, 84600, Muar, Johor, Malaysia; Ceramic and Amorphous Group (CerAm), Faculty of Applied Sciences and Technology, Pagoh Higher Education Hub, Universiti Tun Hussein Onn Malaysia, 84600, Panchor, Johor, Malaysia.
Mohd Hafiz Mohd Zaid: Department of Physics, Faculty of Science, Universiti Putra Malaysia, 43400, UPM Serdang, Selangor, Malaysia
Khaled Althubeiti, Mohammed Aljohani: Department of Chemistry, College of Science, Taif University, P.O. BOX. 110, 21944, Taif, Saudi Arabia

1 Introduction

The world population is increasing, so clean, purified drinkable water demand is also increasing day by day because clean water is essential for the survival of human life. The establishment of industries is also increasing to fulfill the requirements of the global population necessary daily life things but their effluent contains different organic and inorganic pollutants that affect the quality of drinking water and eventually disturb the environment and ecology system [1,2]. Among the different pollutants of industrial discharge, non-biodegradable organic and inorganic dyes are one of the effluents that cause water pollution, which can have serious repercussions. To address this serious problem, different physical, chemical, and biological techniques were used to treat the water; however, these efforts failed due to the hazardous contaminants could not be fully mineralized or expensive setup [3]. The failure of all approaches has caused researchers to focus on the creation of simple, affordable, and innovative techniques that have the potential to completely remediate wastewater [4,5]. Consequently, photocatalysis based on the advanced oxidation process has emerged as an efficient and promising approach for the degradation of both organic and inorganic pigments [6]. For photocatalytic applications, researchers have focused on heterostructure two-dimensional (2D) transition metal dichalcogenides (TMDs) and transition metal oxides (TMOs) such as phosphates, sulfides, carbides, and nitrides [7–9].

The diverse range of applications of TMOs in supercapacitors, sensors, transistors, and photocatalysis has garnered significant interest. Vanadium pentoxide (V_2O_5) is among the most extensive and potential materials considered as a TMOs. V_2O_5 is a common TMO material that has good ion or molecular interaction, is inexpensive, naturally abundant, and has a high guest cation density [10,11]. However, low electrical conductivity, sluggish electrochemical kinetics, poor electrochemical stability, and substantial volume expansion during cycling are problems with bulk V_2O_5 with dense shapes [12].

Among the various 2D photocatalyst materials, layered structured molybdenum disulfide (MoS_2) has attained the most attention due to earth-abundant composition, increased stability, and proficient activity to the improvement of various MoS_2-based photocatalysts [13]. Nevertheless, the transition metal sulfides' reduced stability and active surface sites severely limited their efficiency to function as effective photocatalysts [14,15]. Therefore, MoS_2, in combination with other materials, like V_2O_5, forms heterointerfaces that benefit from the abundance of V═O and can enhance active intermediates (OOH*) by controlling the valence electron structure of V element and stabilizing the oxygen sites within the atomic network [16]. This is made possible by the subsistence of multivalent states of the V element. TMD materials such as MoS_2 with the general formula AX_2 where A is a transition metal such as Ni, Cr, Co, Ru, and Mo, and X indicates Te, Se, or S. Many studies have been found to reduce MoS_2 limitations by creating a composite or heterogeneous structure to reduce recombination rates, increasing conductivity by inclusion with anion, and charge carrier transformation [17,18]. The chemical formulation of MoS_2 is about 59.94% molybdenum (Mo) and 40.05% sulfur (S) with weight percentages, respectively. MoS_2 is 5.069 g cm^{-3} denser and possesses a molar mass of about 160.07 g mol^{-1}. MoS_2 can produce dry lubricating coating and generally possesses outstanding chemical and thermal stability [19,20]. The catalytic activity of MoS_2 nanoparticles (NPs) is highly conductive, and their physical characteristics are outstanding [21]. MoS_2 is more reactive, has a greater adsorption capacity, and has a larger active surface area than bulk materials. Although MoS_2 material is stable in aqueous conditions, its applicability in the solar spectrum is limited. An excellent photocatalyst must have the following essential characteristics: maximal absorption with extensive surface active site area in the visible light spectrum, ideal band edges for initiating reactions, friendliness toward the environment, cheap cost, good stability, and sustainability [22–25].

When $V_2O_{5(1-x)}MoS_{2(x)}$ (X = 1–5% w/w) nanocomposites are bombed with a radiant light source (450 nm continuous diode laser), the nanocomposites resistance becomes less intense with small resistance to the nanocomposite pellets. Excessive exposure to laser beams leads to tuning the distinctive properties [26]. The higher binding rate is due to the higher energy given through laser exposure to the nanocomposites, causing its chemical and structural changes. The restructuring process may be enhanced by incorporating MoS_2 NPs into the V_2O_5 matrix for light absorption due to tuning of energy bandgap.

Here, in the present research, the hydrothermal technique was used to synthesize 2D-layered heterostructure $V_2O_{5(1-x)}MoS_{2(x)}$ (X = 1–5% w/w) nanocomposites with high uniformity, homogeneity, and controllable size. The novelty of this study is that a continuous diode laser has been used to irradiate MoS_2-doped V_2O_5 nanocomposites for 2, 4, 6, 8, and 10 min, respectively, to tune various properties by reconstructing material layers for enhancement of photocatalytic applications. According to photocatalytic studies, the large active sites for light absorption, decrease in the electron–hole pair recombination rate, and increase in charge transportation, respectively, enable the as-prepared $V_2O_{5(1-x)}MoS_{2(x)}$ (X = 1–5% w/w) composite catalysts

to exhibit effective catalytic performance for water degradation. When compared to its separate materials, the 2D heterostructured layered $V_2O_{5(1-x)}MoS_{2(x)}$ (X = 1–5% w/w) composite exhibits low over-potential and high stability. Therefore, due to its excellent conductivity, highly exposed catalytically active sites, and the cooperatively formed reconstructed 2D-layered heterostructures MoS_2-doped V_2O_5, it exhibits superior activity that is easily reproducible for a variety of applications such as carbon dioxide (CO_2) reduction, water splitting, hydrogen (H_2) production, nitrogen (N_2) fixation, *etc.* Thus, synthesized layered heterostructures $V_2O_{5(1-x)}MoS_{2(x)}$ (X = 1–5% w/w) nanocomposites demonstrated exceptional increased electrochemical characteristics and great photocatalytic applicability.

2 Experimental method and laser setup

2.1 Preparation of sample

Hydrothermal process was used to synthesize a $V_2O_{5(1-x)}MoS_{2(x)}$ (X = 1–5% w/w) nanocomposite. For the preparation of the MoS_2-doped V_2O_5 nanocomposite, MoS_2 and V_2O_5 NPs was prepared separately. First, dissolve 2.285 g ammonium heptamolybdate tetrahydrate and 1.1 g thiourea in 70 mL of de-ionized (DI) water, which was then agitated for 30 min. With the use of a 500 mL Teflon line autoclave, the resultant mixture was placed in the furnace at 180–200°C for 48 h to eliminate residual solution, as shown in Figure 1. After being allowed to cool to ambient temperature, the obtained samples were cleaned with ethanol and DI water and stored in centrifuge tubes. After being baked for 12 h at 60°C, the final MoS_2 precipitate samples were dried. For the preparation of V_2O_5 NPs, 1 g of salt ammonium metavanadate NH_4VO_3 was dissolved in 20 mL of hydrogen peroxide. Furthermore, this mixture was kept in a magnetic stirrer for stirring for 60 min. After stirring, a homogeneous mixture was obtained. The homogeneous mixture was autoclaved for 48 h at 200˚C, as shown in Figure 1. HNO_3 was used to maintain the pH of the solution. The obtained sample was placed in open air to cool. In the end, the obtained precipitate was dried in the oven for about 6 h at 80°C. The final product V_2O_5 NPs was dried into nanopowder form. For the synthesis of $V_2O_{5(1-x)}MoS_{2(x)}$ (X = 1–5% w/w) nanocomposite, V_2O_5 and MoS_2 were first synthesized in a nanomaterial form. These nanomaterials were dissolved in 20 mL ethanol solution. Furthermore, the obtained homogeneous mixture was stirred using a magnetic stirrer for 12 h at room temperature. After stirring, the obtained product was placed in a sonicater for 2 h. The obtained sample was dried in an oven at 60°C for 12 h. In the end, the nanocomposite of MoS_2-doped V_2O_5 precipitate was calcinated for 3 h at 250°C.

2.2 Laser exposure setup

The continuous diode laser had a maximum mean laser power of 20 W. The continuous pulse produced visible light with a wavelength of 450 nm, as shown in Figure 2. The

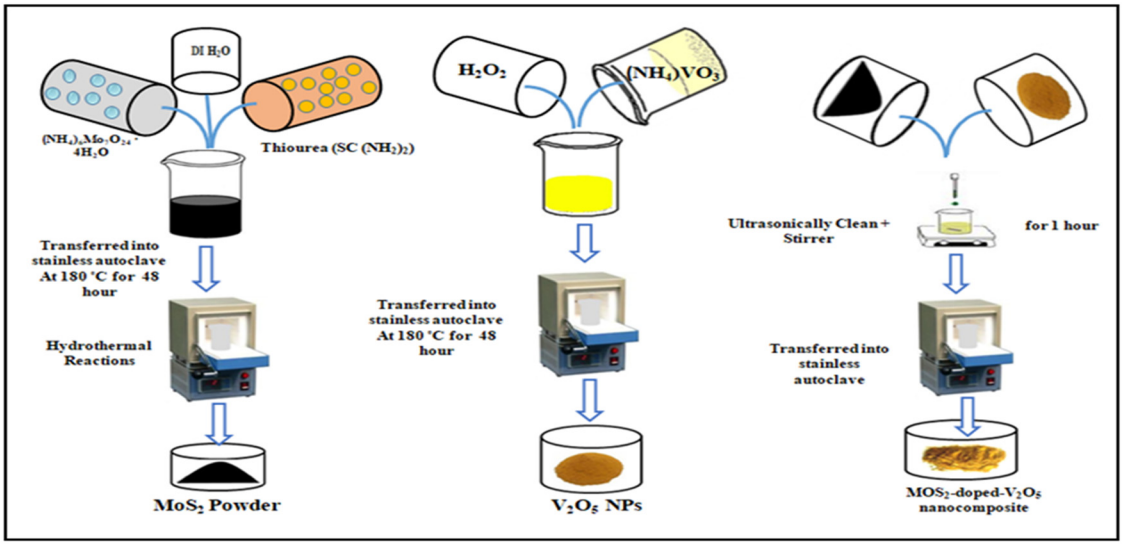

Figure 1: Experimental diagram of hydrothermally synthesized $V_2O_{5(1-x)}MoS_{2(x)}$ (X = 1–5% w/w) nanocomposites.

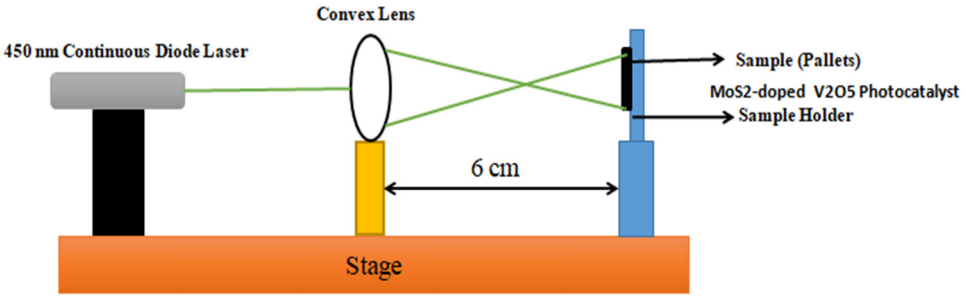

Figure 2: The experimental setup of laser irradiation into $V_2O_{5(1-x)}MoS_{2(x)}$ (X = 1–5% w/w) nanocomposite for tuning of different properties.

laser and MoS_2-doped-V_2O_5 nanocomposites pallets were separated by 6 cm, allowing the continuous laser light to cover almost 1 × 1 cm^2 of the pallet surface. The continuous laser lights were irradiated at the MoS_2-doped V_2O_5 nanocomposite pallets. The duration of laser exposure was 2, 4, 6, 8, and 10 min. Laser irradiation can tune the energy band gap and light absorption for photocatalytic applications.

3 Results and discussion

3.1 XRD phase analysis

A Philips X-ray diffraction was used to capture X-ray diffraction (XRD) patterns using Ni-filtered Cu-Kα radiation. The average crystallite size and phase formation of laser-irradiated pure V_2O_5 and $V_2O_{5(1-x)}MoS_{2(x)}$ (X = 1–5% w/w) nanocomposites were observed using a X-ray diffraction, as shown in Figure 3. The crystallite sizes of pure V_2O_5 and MoS_2-doped-V_2O_5 nanocomposites decreased from 42.53 to 22.89 nm with increasing MoS_2 percentage as well as laser irradiation exposure time, respectively, as shown in Table 1. The observed peaks at 2θ values 10.12°, 16.45°, 20.15°, 24.45°, 29.06°, 33.32°, and 44.35° are well coordinated to the (002), (200), (001), (101), (110), (400), (011), and (210) *hkl* plane of MOS_2-doped-V_2O_5, which are in accordance with JCPDS No. 37-1492 and No. 41-1426, respectively, as shown in Figure 3. There were no impurity peaks, indicating the purity of the $V_2O_{5(1-x)}MoS_{2(x)}$ (X = 1–5% w/w) nanocomposites and their excellent crystalline nature. Weight percentage increases caused the distinctive peaks to shift toward a lower angle. The Debye–Scherrer equation was utilized to determine the NPs' crystallite size [27].

$$D = \frac{K\lambda}{\beta \cos\theta}, \tag{1}$$

where β is the full width at half maximum (FWHM) of the XRD peak that appears at the diffraction angle θ, D is the crystallite size, θ is the Bragg diffraction angle, and λ is the X-ray wavelength (Cu-Kα radiation = 1.54 Å) [28]

$$d = \frac{\lambda}{2\sin\theta}, \tag{2}$$

where Θ is the Bragg diffraction angle, λ is the X-ray wavelength (Cu-Kα radiation = 1.54 Å), and d is the d-spacing. Lattice constants values increased slightly due to the increased weight percentage of MoS_2 in the $V_2O_{5(1-x)}MoS_{2(x)}$ (X = 1–5% w/w) nanocomposites. Thus, an increase in the lattice constant is associated with a lattice increment in cell volume (V_{cell}) as the weight percentage of MoS_2 in the crystal structure increases.

Also, as observed by XRD peaks, the average particle size of laser-irradiated pure V_2O_5 and $V_2O_{5(1-x)}MoS_{2(x)}$ (X = 1–5% w/w) nanocomposites tends to decrease, increasing surface area and decreasing the rate at which electron–hole pairs

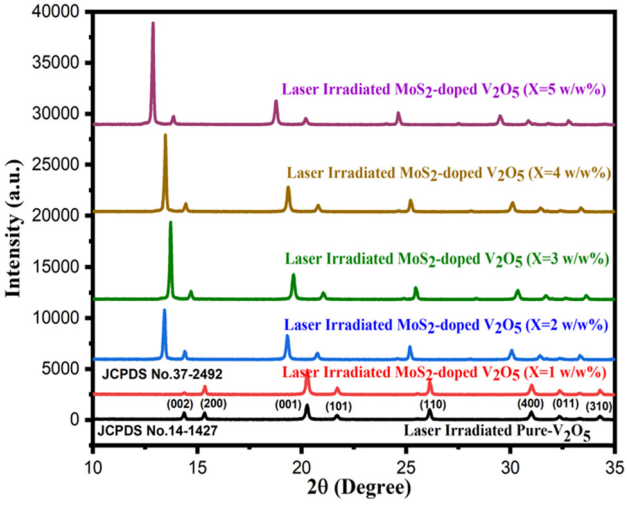

Figure 3: The phase analysis pattern of laser irradiated $V_2O_{5(1-x)}MoS_{2(x)}$ (X = 1–5% w/w) nanocomposites.

Table 1: Structural parameters of laser irradiated $V_2O_{5(1-x)}MoS_{2(x)}$ (X = 1–5% w/w) nanocomposite

Nanocomposites	Irradiation time (min)	2θ (°)	FWHM	Miller indices (*hkl*)	*d*-spacing (Å)	Average crystallite size *D* (nm)
Pure-V_2O_5	0	13	0.1322	002	2.6421	42.53
$V_2O_{5(1-x)}MoS_{2(x)}$ (X = 1% w/w)	4	15	0.3685	200	2.5341	36.66
$V_2O_{5(1-x)}MoS_{2(x)}$ (X = 2% w/w)	8	20	0.4557	001	2.34567	32.33
$V_2O_{5(1-x)}MoS_{2(x)}$ (X = 3% w/w)	12	26	0.7548	101	2.01489	28.44
$V_2O_{5(1-x)}MoS_{2(x)}$ (X = 4% w/w)	16	31	0.8811	400	1.96289	25.24
$V_2O_{5(1-x)}MoS_{2(x)}$ (X = 5% w/w)	20	32	0.8956	011	1.95161	22.89

recombine. This increases photon light absorption and accelerates the degradation of organic dyes. As a result, photocatalysis would be more effective at gathering light and be better able to break down industrial colors like methylene blue (MB) in contaminated water.

3.2 Elemental compositional analysis (EDX)

The chemical compositions of laser irradiated pure V_2O_5 and $V_2O_{5(1-x)}MoS_{2(x)}$ (X = 1–5% w/w) nanocomposites are analyzed hydrothermally using EDX spectroscopy, as illustrated in Figure 4(a–f). The presence of vanadium (V), oxygen (O), and gold (Au) with respective atomic weights of 70.84, 28.36, and 0.80% is shown by the EDX peaks of pure V_2O_5 in Figure 4(a). The X-ray diffraction peaks in the V_2O_5 lattice system demonstrate that MoS_2 replacements were successful, and this was validated by the acquired EDX data. Vanadium (V), oxygen (O), aluminum (Al), molybdenum (Mo), sulfur (S), and gold (Au) with atomic weight percentages of 80.89, 16.25, 1.87, 2.09, and 0.90% are displayed by the EDX peaks in Figure 4(b). The vanadium (V), oxygen (O), aluminum (Al), molybdenum (Mo), sulfur (S), and gold (Au) EDX peaks in Figure 4(c–f) demonstrate that these elements have varying atomic weight percentages as shown in Table 2.

3.3 X-ray photoelectron spectroscopy (XPS)

The surface texture of a MoS_2-doped V_2O_5 nanocomposite was examined using XPS in relation to the presence of various components, chemical structures, chemical oxidation states, and electron movement. As seen in Figure 5(a), MoS_2 has two peaks at 228.9 and 232.1 eV, which correspond to Mo^{4+} $3d_{5/2}$ and Mo^{4+} $3d_{3/2}$, respectively. These peaks demonstrate the presence of Mo^{4+}, which is an indicator of MoS_2. The shift in the binding energy of Mo 3d in MoS_2-doped V_2O_5 composite further indicates a strong synergistic effect between Mo and V metals in MoS_2-doped V_2O_5 composite photocatalyst and suggests a notable electronic structure difference in Mo between MoS_2 and MoS_2-doped V_2O_5 composite photocatalyst. The presence of S_{2-} in MoS_2 is demonstrated by the peaks for S $2p_{3/2}$ at approximately 161.7 eV and S $2p_{1/2}$ at 162.9 eV in Figure 5(c). The four peaks are associated with the V 2p spectrum, which is shown in Figure 5(b). Two of the peaks correspond to the V^{5+} values V $2p_{1/2}$ at 524.5 eV and V $2p_{3/2}$ at 516.9 eV. The remaining two significant peaks, which are located at 523.1 eV and 515.3 eV, respectively, are consistent with 2 $p_{1/2}$ and 2 $p_{3/2}$ of V^{4+} in V_2O_5. It is possible to assume that V^{5+} predominates in the synthesized nanocomposites since V^{5+} peak intensity and area are much bigger than V^{4+} peak. Additionally, as demonstrated in Figure 5(d), the notable peaks of O 1 s at 529.7 and 531.2 eV are indicative of the presence of the V−O functional group of V_2O_5.

3.4 Morphological analysis

Using a JEOL IT800 model of field-emission scanning electron microscopy (FESEM) was used to analyze the surface morphology and shape of hydrothermally prepared laser-irradiated pure V_2O_5 and $V_2O_{5(1-x)}MoS_{2(x)}$ (X = 1–5% w/w) nanocomposites, as shown in Figure 6(a–f). Before being examined with a FESEM, the samples were polished to boost the emissivity of the samples and then gold coated. The samples of $V_2O_{5(1-x)}MoS_{2(x)}$ (X = 1–5% w/w) nanocomposites were shown to have layered structures in the scanning electron microscopy images. The surface morphology of pure V_2O_5 and $V_2O_{5(1-x)}MoS_{2(x)}$ (X = 1–5% w/w) nanocomposites shows that part of the V_2O_5 nanospheres pierced into the MoS_2 layered matrix, while the rest of the nanospheres are arranged in bunches on MoS_2 layers. The average grain size of the laser-irradiated doped composites $V_2O_{5(1-x)}MoS_{2(x)}$ (X = 1–5% w/w) decreased as the doping fraction of MoS_2 increased, but the nanocomposites' shape did not change. Furthermore, small grains emerge as a result of increased nucleation as the V_2O_5 is integrated into the MoS_2 layered structure. The non-homogeneous

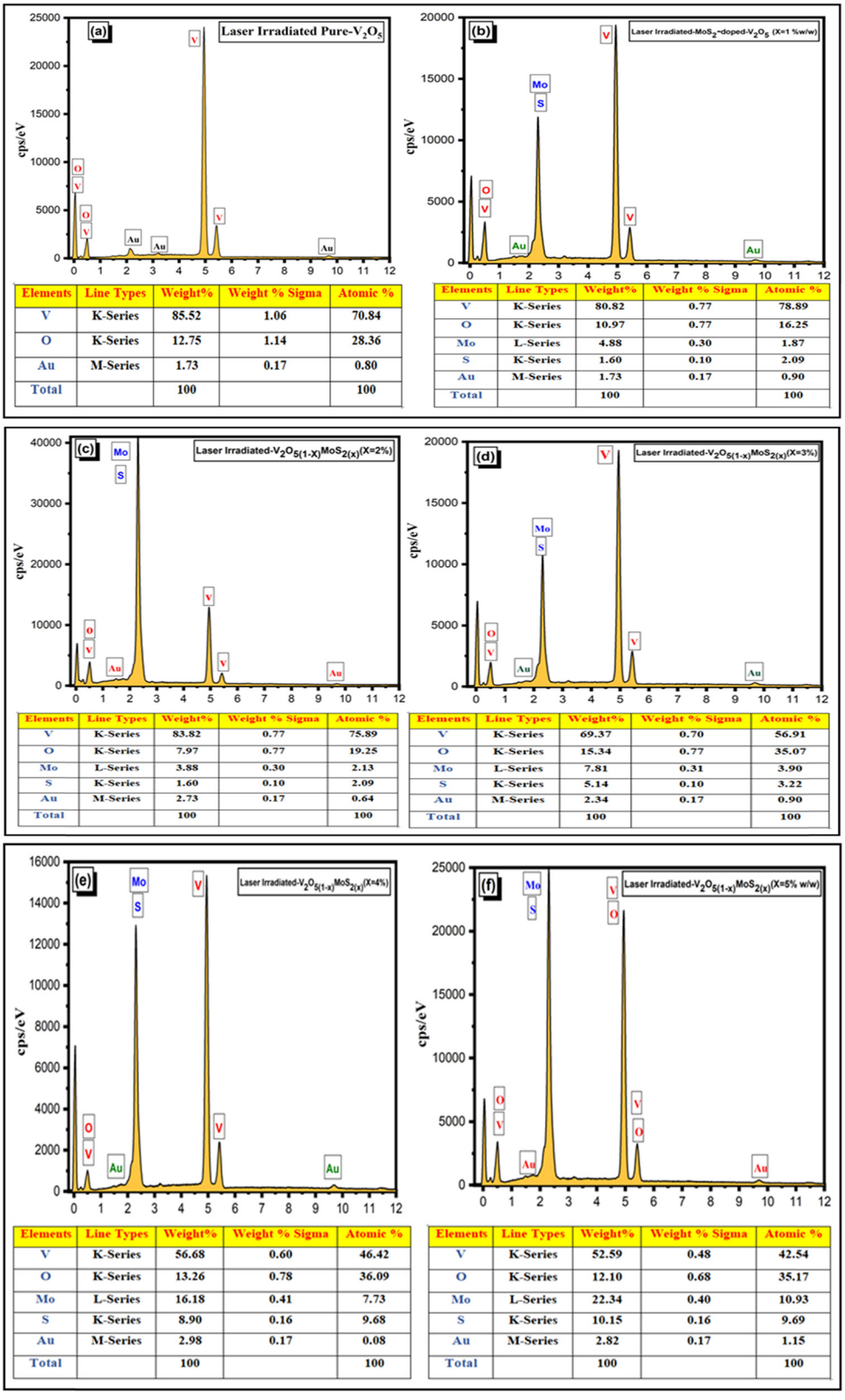

Elements	Line Types	Weight%	Weight % Sigma	Atomic %
V	K-Series	85.52	1.06	70.84
O	K-Series	12.75	1.14	28.36
Au	M-Series	1.73	0.17	0.80
Total		100		100

Elements	Line Types	Weight%	Weight % Sigma	Atomic %
V	K-Series	80.82	0.77	78.89
O	K-Series	10.97	0.77	16.25
Mo	L-Series	4.88	0.30	1.87
S	K-Series	1.60	0.10	2.09
Au	M-Series	1.73	0.17	0.90
Total		100		100

Elements	Line Types	Weight%	Weight % Sigma	Atomic %
V	K-Series	83.82	0.77	75.89
O	K-Series	7.97	0.77	19.25
Mo	L-Series	3.88	0.30	2.13
S	K-Series	1.60	0.10	2.09
Au	M-Series	2.73	0.17	0.64
Total		100		100

Elements	Line Types	Weight%	Weight % Sigma	Atomic %
V	K-Series	69.37	0.70	56.91
O	K-Series	15.34	0.77	35.07
Mo	L-Series	7.81	0.31	3.90
S	K-Series	5.14	0.10	3.22
Au	M-Series	2.34	0.17	0.90
Total		100		100

Elements	Line Types	Weight%	Weight % Sigma	Atomic %
V	K-Series	56.68	0.60	46.42
O	K-Series	13.26	0.78	36.09
Mo	L-Series	16.18	0.41	7.73
S	K-Series	8.90	0.16	9.68
Au	M-Series	2.98	0.17	0.08
Total		100		100

Elements	Line Types	Weight%	Weight % Sigma	Atomic %
V	K-Series	52.59	0.48	42.54
O	K-Series	12.10	0.68	35.17
Mo	L-Series	22.34	0.40	10.93
S	K-Series	10.15	0.16	9.69
Au	M-Series	2.82	0.17	1.15
Total		100		100

Figure 4: (a–f) The EDX of laser irradiated $V_2O_{5(1-x)}MoS_{2(x)}$ (X = 1–5% w/w) nanocomposite.

Table 2: The elemental mapping of laser irradiated $V_2O_{5(1-x)}MoS_{2(x)}$ (X = 1–5% w/w) nanocomposite

Materials name	(V)	(O)	(Mo)	(S)	(Au)
Laser-irradiated-pure-V_2O_5	70.84	28.36	0.00	0.00	0.80
Laser-irradiated $V_2O_{5(1-x)}MoS_{2(x)}$ (X = 1% w/w)	78.89	16.25	1.87	2.09	0.90
Laser-irradiated $V_2O_{5(1-x)}MoS_{2(x)}$ (X = 2% w/w)	75.89	19.25	2.13	2.09	0.64
Laser-irradiated $V_2O_{5(1-x)}MoS_{2(x)}$ (X = 3% w/w)	55.91	35.07	3.90	3.22	0.90
Laser-irradiated $V_2O_{5(1-x)}MoS_{2(x)}$ (X = 4% w/w)	46.42	36.09	7.73	9.68	0.08
Laser-irradiated $V_2O_{5(1-x)}MoS_{2(x)}$ (X = 5% w/w)	42.54	35.17	10.93	9.80	1.67

distribution of V_2O_5 NPs on the MoS_2 layered structure's surface is seen in Figure 6(e–f), and this phenomenon might be related to electrostatic attraction. Additionally, as seen in Figure 6(e–f), the smaller grain size increases surface area, which in turn causes a decrease in the rate at which photogenerated charge carriers recombine and an increase in photon light absorption, which accelerates the degradation of organic dyes.

3.5 Photocatalytic performance under UV–Visible light

The photocatalytic performances of laser-irradiated pure V_2O_5 and $V_2O_{5(1-x)}MoS_{2(x)}$ (X = 1–5% w/w) nanocomposites for MB is shown in Figure 7(a–h), measured using a U-3900H spectrometer. The absorption peaks of MB for 0, 30, 60, 90, 120, and 150 min are described in the UV–Visible

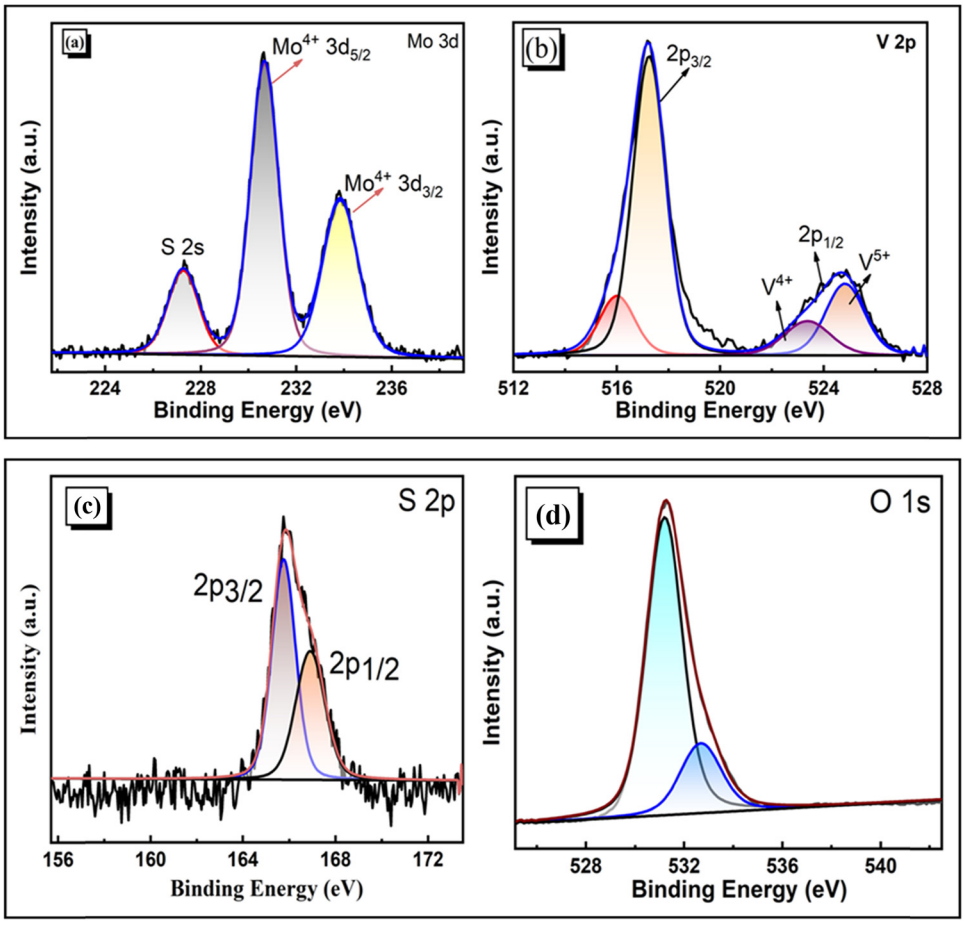

Figure 5: (a–d) XPS spectrum of $V_2O_{5(1-x)}MoS_{2(x)}$ (X = 1–5% w/w) nanocomposite of (a) Mo 3d (b) V 2p (c) S 2p and (d) O 1s.

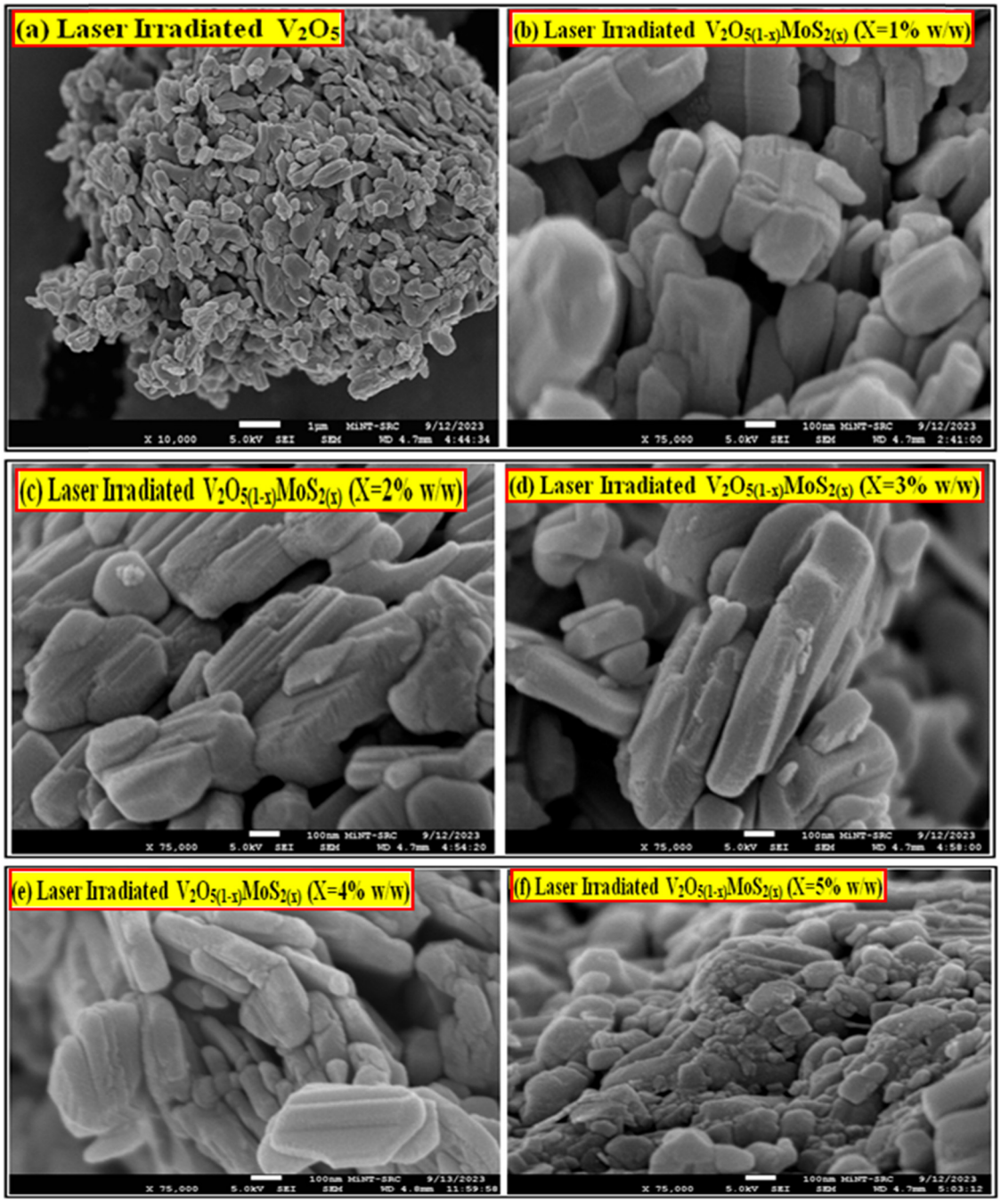

Figure 6: (a–f) Surface morphology analysis of laser irradiated $V_2O_{5(1-x)}MoS_{2(x)}$ (X = 1–5% w/w) nanocomposite.

investigation. Approximately 95% of the MB was degraded after 150 min, and the sharpness of absorption peaks steadily decreased with increasing degradation time of the organic dyes. The maximum MB absorption wavelength shifted from 0 to 150 min as the degradation time increased, as seen by the UV–Visible absorption peaks. This indicates that the structure of MB within 150 min was degraded and the photocatalytic degradation of MB is a mineralization process. To establish an adsorption–desorption equilibrium before photocatalytic degradation, the catalyst adsorbed MB for 30 min while being protected from light. The "dark" tests' findings indicated that the small amount of MB degradation that takes place in the absence of UV–Visible light is caused by photocatalytic degradation. From Figure 7(a–h), it can be observed that in the presence of a catalyst of pure V_2O_5 and $V_2O_{5(1-x)}$

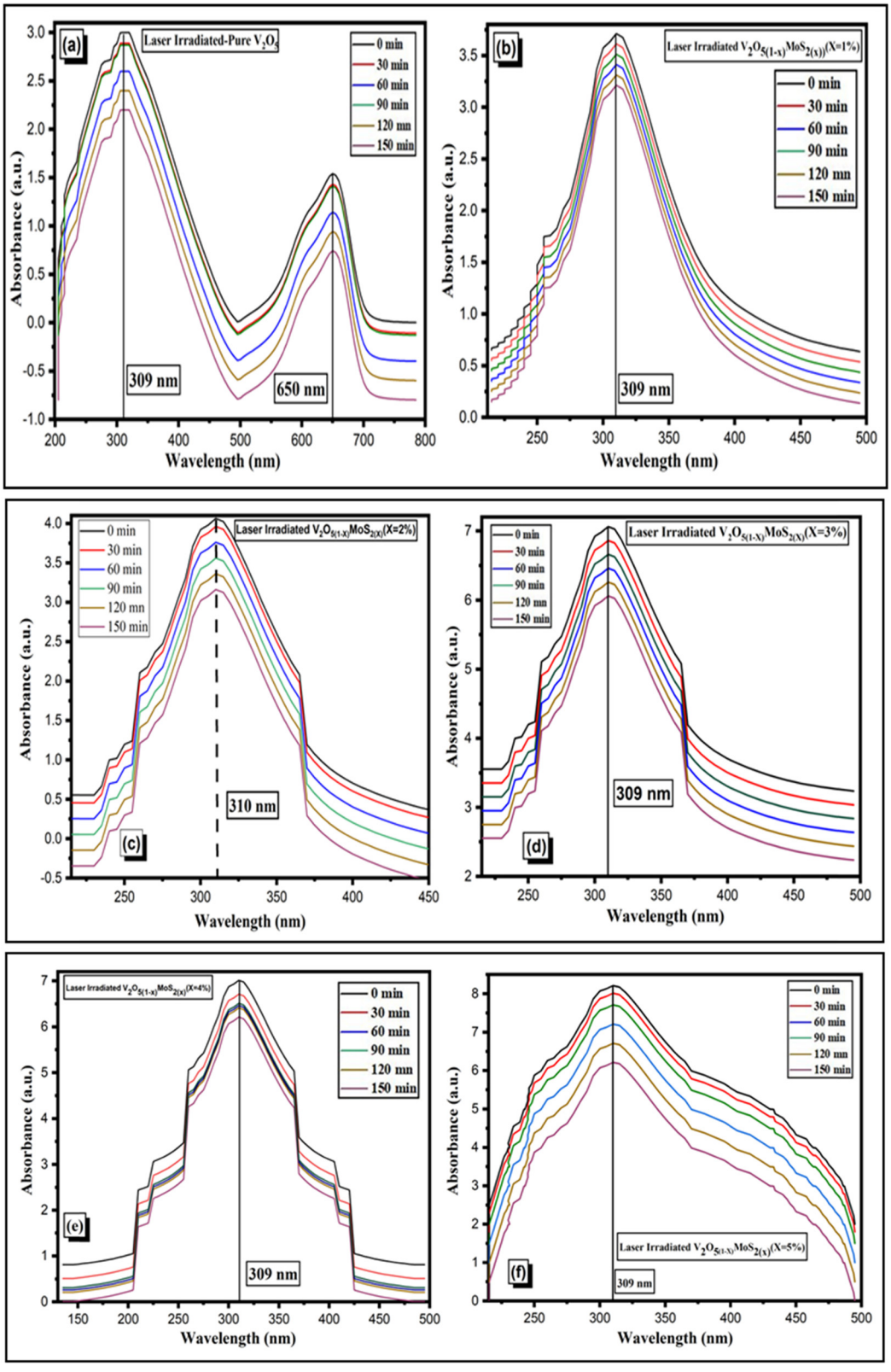

Figure 7: (a–h) Photocatalytic activity of laser irradiated $V_2O_{5(1-x)}MoS_{2(x)}$ (X = 1–5% w/w) nanocomposite.

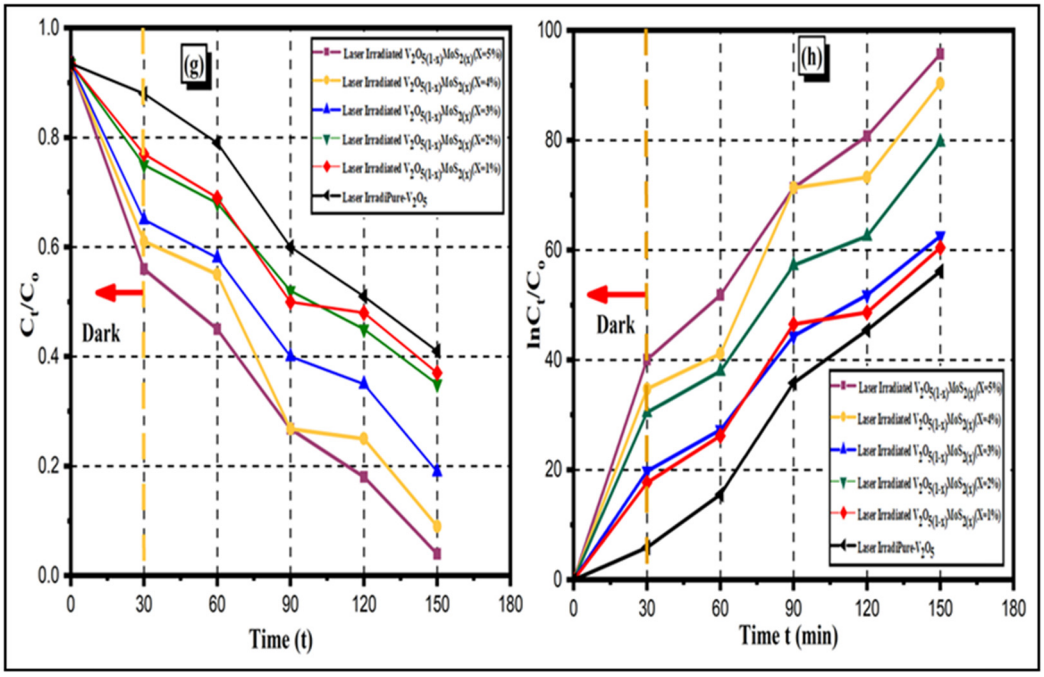

Figure 7: (*Continued*)

$MoS_{2(x)}$ (X = 1–5% w/w) nanocomposites, the degradation percentages of MB were 40.11, 51.40, 70.30, 80.75, and 95.40%, respectively. The degradation percentages of MB are increased with an increase of the doping percentage of MoS_2 from 1 to 5% w/w as well as laser irradiation. According to this, the amount of MB that is degraded by catalyst $V_2O_{5(1-x)}MoS_{2(x)}$ (X = 1–5% w/w) nanocomposites is more than it is when using pure V_2O_5. After 120 min of remediation, the greatest deteriorated percentage (95.40%) was tested using catalyst $V_2O_{5(1-x)}MoS_{2(x)}$ (X = 1–5% w/w) composites. This nanocomposite demonstrated improved photocatalytic activity. This is consistent in line with the analysis's conclusions, which are shown in Figure 7(a–h). Based on the simulated curve, there is a solid linear connection between the degradation time and $\ln(C_t/C_0)$. A pseudo-first-order kinetic model with a degree of fit of 0.9501 (R^2) illustrates the photocatalytic degradation of MB in the following formulas [29]:

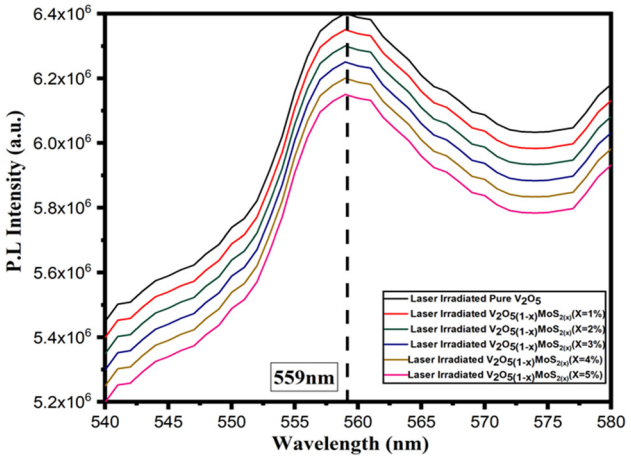

Figure 8: PL spectra of laser irradiated $V_2O_{5(1-x)}MoS_{2(x)}$ (X = 1–5% w/w) nanocomposites.

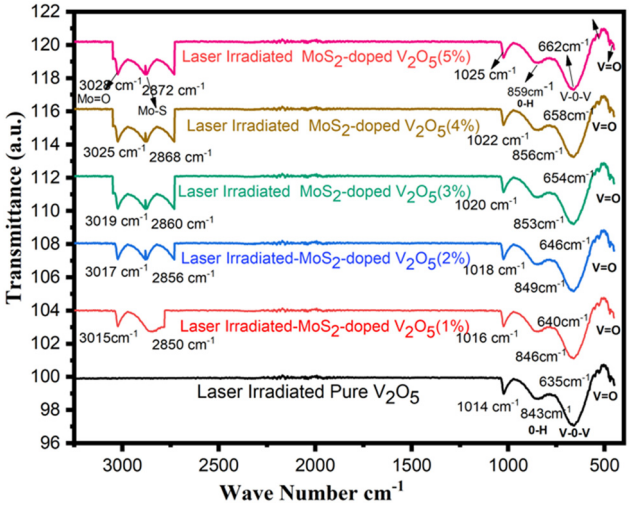

Figure 9: Functional group analysis of laser irradiated $V_2O_{5(1-x)}MoS_{2(x)}$ (X = 1–5% w/w) nanocomposites.

Table 3: Different functional groups of laser irradiated $V_2O_{5(1-x)}MoS_{2(x)}$ (X = 1–5% w/w) nanocomposites

Functional groups	Laser-irradiated pure-V_2O_5 (cm^{-1})	Laser-irradiated MoS_2-doped-V_2O_5 (1%) (cm^{-1})	Laser-irradiated MoS_2-doped-V_2O_5 (2%) (cm^{-1})	Laser-irradiated MoS_2-doped-V_2O_5 (3%) (cm^{-1})	Laser-irradiated MoS_2-doped-V_2O_5 (4%) (cm^{-1})	Laser-irradiated MoS_2-doped-V_2O_5 (5%) (cm^{-1})
O–H	843	846	849	853	856	859
V–O–V	633	636	640	646	654	658
O═V	456	459	461	465	467	470
Mo–S	None	2,850	2,856	2,860	2,868	2,872
Mo═O	None	3,015	3,017	3,019	3,025	3,028

$$-\ln\left(\frac{C_t}{C_o}\right) = kt, \tag{3}$$

where k is the rate constant, C_t is the MB concentration at time t, and C_0 is the MB starting concentration. The k value of MB was calculated to be 0.0021 min^{-1} for complete $V_2O_{5(1-x)}MoS_{2(x)}$ (X = 1–5% w/w) samples.

3.6 Photoluminescence (PL)

PL characteristic was performed, as shown in Figure 8, to investigate the ability of electrons (e^-) and hole (h^+) pairs separation. According to PL's findings, a lower photocatalyst intensity (PL) peak is indicative of a slower rate of electron–hole recombination, which increases separation capacity. This result indicates that the dye-degrading capacity of laser irradiated $V_2O_{5(1-x)}MoS_{2(x)}$ (X = 1–5% w/w) nanocomposites is growing with increasing substitution percentage and shows well-organized charge transfer on the photocatalyst surface. The laser irradiated $V_2O_{5(1-x)}MoS_{2(x)}$ (X = 1–5% w/w) nanocomposites' PL peaks clearly show a decrease in intensity as the MoS_2 doping percentage increases. This indicates that the laser-irradiated MoS_2-doped-V_2O_5 nanocomposites have higher photogenerated electrons (e^-) and hole (h^+) pairs, which enhances photocatalytic application.

3.7 Fourier transformation infrared spectroscopy (FTIR)

A Perkin Elmer spectrum 100 FTIR spectrometer is used to determine potential functional groups present in laser-irradiated $V_2O_{5(1-x)}MoS_{2(x)}$ (X = 1–5% w/w) and pure V_2O_5 nanocomposites. The crystal vibration modes and ion locations of laser-irradiated MoS_2-doped-V_2O_5 nanocomposites may be determined using the FTIR approach. The FTIR method may be used to determine the ion locations and crystal vibration modes of both laser-irradiated pure V_2O_5 and $V_2O_{5(1-x)}MoS_{2(x)}$ (X = 1–5% w/w) nanocomposites. Figure 9 shows the FTIR spectra of laser irradiated pure V_2O_5 and $V_2O_{5(1-x)}MoS_{2(x)}$ (X = 1–5% w/w) that were obtained between 250 and 3,200 cm^{-1}. Vanadium–oxygen and molybdenum–sulfur bonds bending and stretching correspond to the unique characteristics of the 250–3,200 cm^{-1}. The large band at 843–859 cm^{-1} is created by the O–H stretching from water, whereas the absorption bands at 941 cm^{-1} are ascribed to the OH bending. The absorption bands at 1,014–1,025 cm^{-1} are responsible for the C–H bending. The small bands at 2,850–2,872 and 3,015–3,028 cm^{-1} are created by Mo–S and Mo═O by the MoS_2 are described by bending bands. The vanadium-oxygen bonds were shifted by the MoS_2 doping and laser irradiation. As shown in Table 3, the absorption peaks are shifted toward higher wavelengths as a result of an increase in MoS_2 doping concentration and laser irradiation time. While doped MoS_2-doped-V_2O_5 is assigned to the bands at 537 to 617 cm^{-1} range, associated with symmetric stretching vibration of V–O–V is located at band 635–662 cm^{-1} for pure-V_2O_5. The optimal integration of MoS_2 into the V_2O_5 host material results in an increase in transmittance intensities. The increase in intensities leads to the stability of laser-irradiated $V_2O_{5(1-x)}MoS_{2(x)}$ (X = 1–5% w/w) nanocomposites.

3.8 Atomic force microscopy (AFM)

The AFM results of laser irradiated pure V_2O_5 and $V_2O_{5(1-x)}MoS_{2(x)}$ (X = 1–5% w/w) nanocomposites are seen in three dimensions by using a BRUKER model dimension edge with scan system as shown in Figure 10(a–e). Table 4 presents the topographical characteristics, including image surface area, image projected surface area, average roughness (R_a), and root mean square roughness (R_q). As shown in Table 4, increasing the doping concentrations of $V_2O_{5(1-x)}MoS_{2(x)}$ (X = 1–5% w/w) results in a decrease in roughness of 58.70,

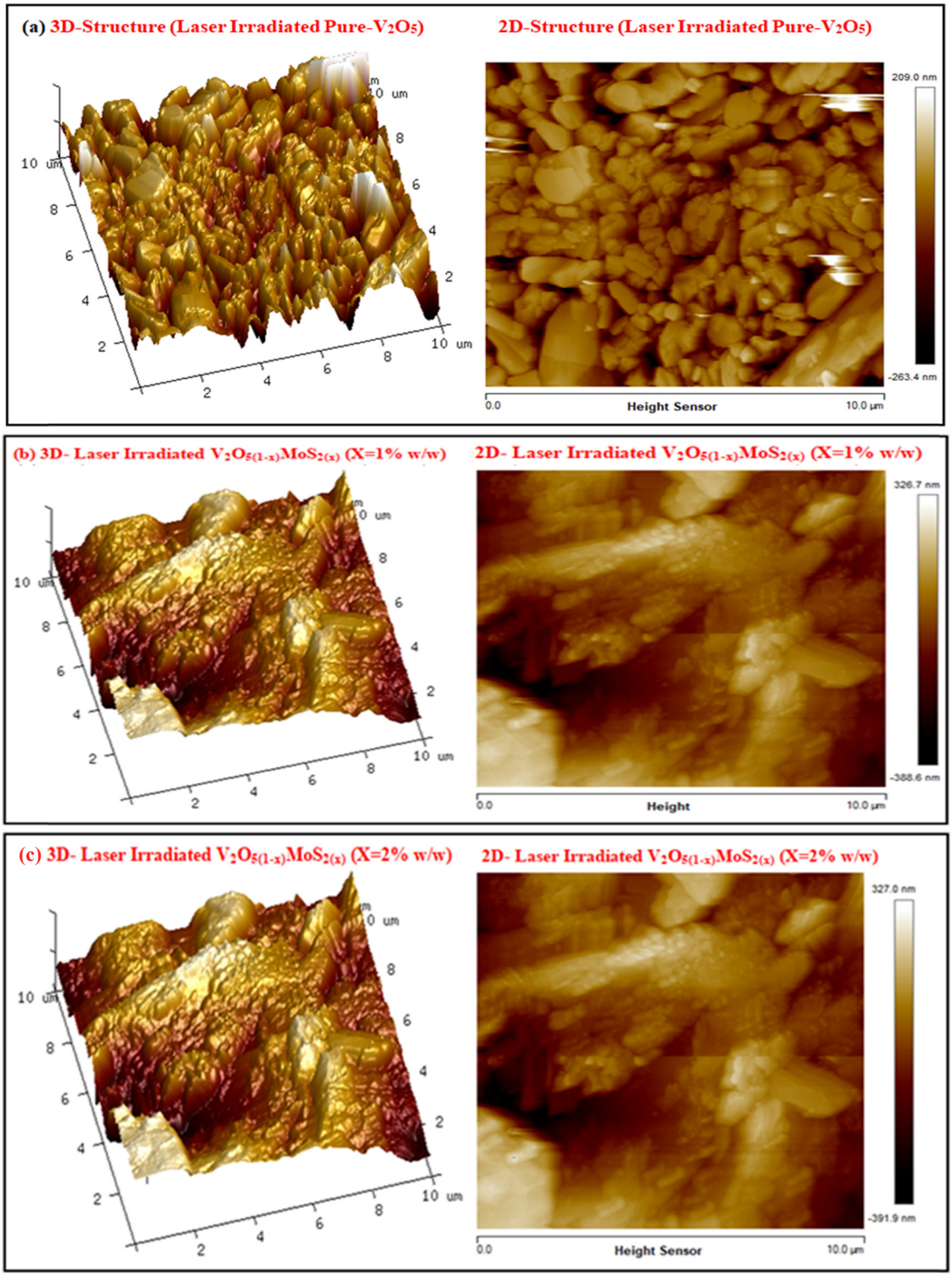

Figure 10: (a–f) Surface analysis through AFM of laser irradiated $V_2O_{5(1-x)}MoS_{2(x)}$ (X = 1–5% w/w) nanocomposites.

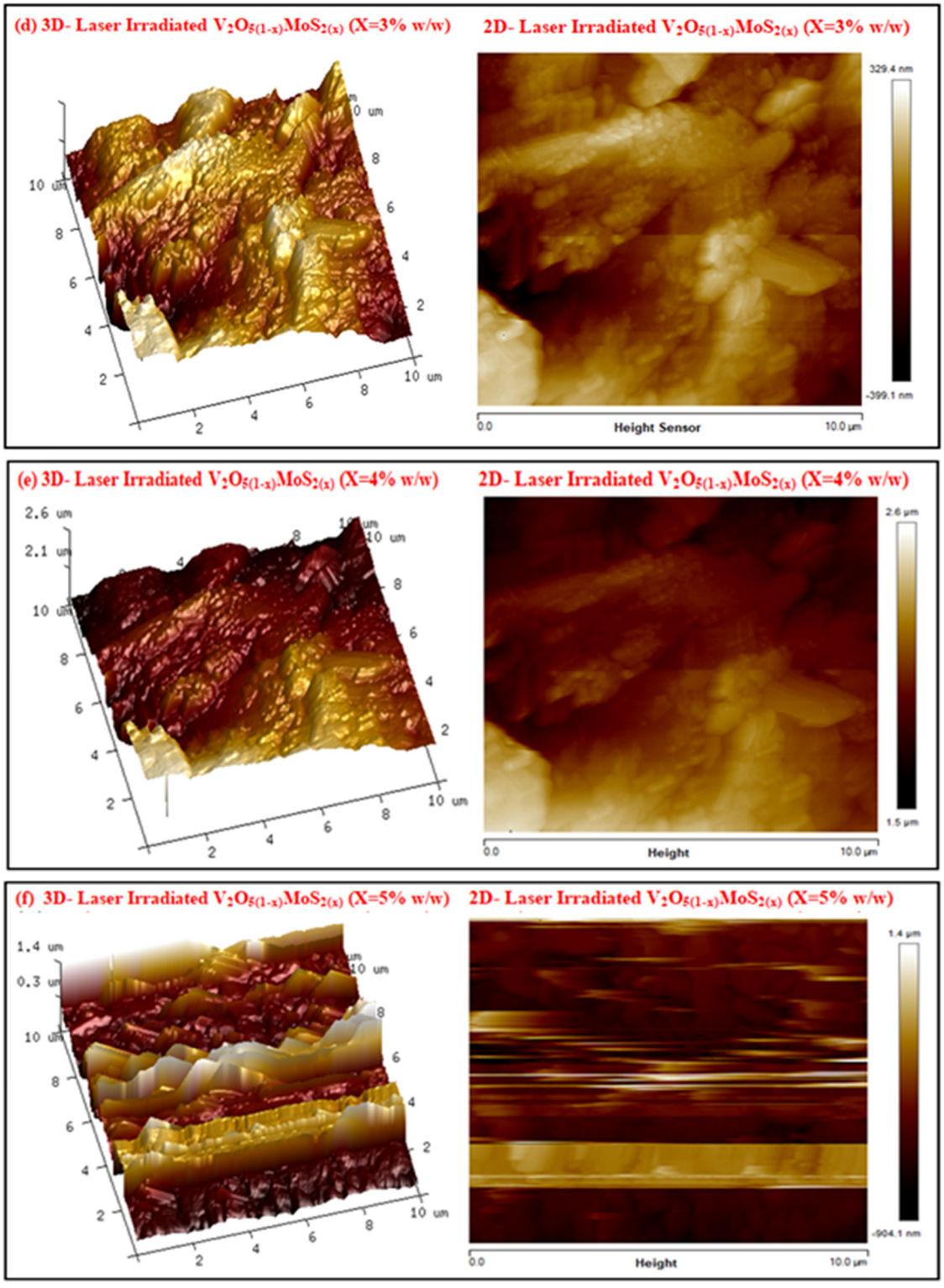

Figure 10: (*Continued*)

Table 4: Different surface parameters of laser irradiated $V_2O_{5(1-x)}MoS_{2(x)}$ (X = 1–5% w/w)

Samples	Image surface area (μm)^2	Image projected surface area (μm)^2	Root mean square roughness R_q (nm)	Average roughness R_a (nm)
Laser-irradiated pure-V_2O_5	108	100	58.70	71.33
Laser-irradiated $V_2O_{5(1-x)}MoS_{2(x)}$ (X = 1% w/w)	125	100	41.36	35.41
Laser-irradiated $V_2O_{5(1-x)}MoS_{2(x)}$ (X = 2% w/w)	133	100	32.11	29.41
Laser-irradiated $V_2O_{5(1-x)}MoS_{2(x)}$ (X = 3% w/w)	141	100	29.23	27.44
Laser-irradiated $V_2O_{5(1-x)}MoS_{2(x)}$ (X = 4% w/w)	151	100	26.21	25.33
Laser-irradiated $V_2O_{5(1-x)}MoS_{2(x)}$ (X = 5% w/w)	169	100	21.22	18.14

41.36, 32.11, 29.23, 26.21, and 21.22 nm. When MoS_2 doping weight percent of MoS_2 is increased, the surface area of layered structured nanocomposites increases from 108, 125, 133, 141, 151, and 169 μm^2. By increasing the weight percent of MoS_2 in $V_2O_{5(1-x)}MoS_{2(x)}$ (X = 1–5% w/w) nanocomposites, the number of layers is likewise growing. According to AFM results, increment in active site surface area, which in turn causes a decrease in the rate at which photogenerated charge carriers recombine and an increase in photon light absorption, which accelerates the degradation of organic dyes.

3.9 Dielectric characteristics

An impedance analyzer called the keysight E49918 was used to evaluate the sample's electrical conductivity for MoS_2-doped-V_2O_5 (about 76 mm thick and 13 mm diameter) at a frequency range of 1 MHz to 3 GHz. The pressure was adjusted by using Keysight 16453A with 1 MHz–1 GHz dielectric material test fixture and ±42 peak output. The Keysight E4991B test head was used as an RF out port. The conductivity measurements were completed at room temperature by using $\sigma = d/AR$. The values of ionic conductivity were calculated using the formula where d is the sample thickness, A is the electrode area, and R is the sample resistance.

3.9.1 Dielectric constants

Generally, dielectric relaxation originates from the mobility of the electric dipole that the applied electric field produces. The Debye–Scherer relaxation model has been used to describe the effects of applied electric field on dielectric materials. The following formula is used to calculate the complex dielectric constant [30]:

$$e^* = e' + j\epsilon''. \tag{4}$$

Dielectric materials can be used to improve the capacity of charge storage. As a result, the capacitance of the material and its dielectric constant are proportionate [31].

$$\epsilon' = \frac{Cd}{\in_0 A}, \tag{5}$$

where A stands for area, C for capacitance, d for thickness, and $\in_0$ for the permittivity of free space. The thickness for $V_2O_{5(1-x)}MoS_{2(x)}$ (X = 1–5% w/w) composite pellets with doping different percentages 1–5% w/w were 1.58, 1.41, 1.68, 1.74, and 1.82 nm, respectively, measured by digital

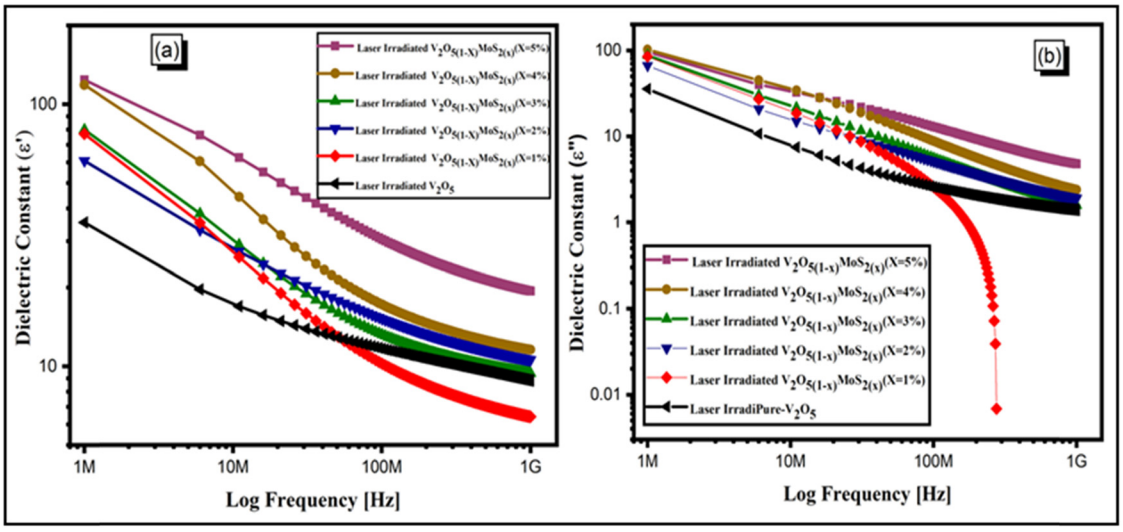

Figure 11: (a, b) Dielectric constants of laser irradiated of $V_2O_{5(1-x)}MoS_{2(x)}$ (X = 1–5% w/w) nanocomposites.

Vernier calipers. The variation of real dielectric function (RDF) (ε') and imaginary dielectric function (IDF) (ε'') with the frequency of laser irradiated of pure V_2O5 and MoS_2-doped-V_2O_5 nanocomposites as shown in Figure 11. The dielectric constant (RDF) ε' is quite high at low frequencies and decreases sharply with increasing frequency and MoS_2 doping percentages. Dipolar polarization, interfacial polarization (IP), atomic polarization, and electronic polarization are the four polarization types that affect a material's dielectric behavior. Dipolar and IPs are highly dependent on frequency and temperature, whereas electronic and ionic polarizations occur at very high frequencies. Charge carrier is affected by applied frequency variations because these polarization processes have a distinct relaxation time. All polarization processes are involved at low applied frequencies, but as the frequency increases, polarization decreases. As the frequency increased, the different dipoles inside the V_2O_5 and $V_2O_{5(1-x)}MoS_{2(x)}$ (X = 1–5% w/w) nanocomposites were unable to follow the electric field; thus, the polarization reduced and therefore ε' decreased. Laser-irradiated pure V_2O5 and $V_2O_{5(1-x)}MoS_{2(x)}$ (X = 1–5% w/w) nanocomposites' distinct dipoles were unable to follow the electric field as the frequency increased, which resulted in a decrement in polarization and dielectric constants (RDF) ε' decreased with increased of doping percentages. The dielectric constant (RDF) ε' values were found to be dependent on the strength of the electrostatic interaction force between the V_2O_5 and $V_2O_{5(1-x)}MoS_{2(x)}$ (X = 1–5% w/w) nanocomposites (synthesized at varying doping percentages) and the functional group in the blend chain of V_2O_5 and $V_2O_{5(1-x)}MoS_{2(x)}$ (X = 1–5% w/w), which facilitates/restricts molecular movement. As a result, in comparison to pure V_2O_5, the doped nanocomposites' effective dielectric polarization at 5% was either enhanced/decreased.

Furthermore, the IP peak, also known as the Maxwell–Wagner–Sillars effect, was visible in the lower frequency range of the IDF (ε'') of laser-irradiated V_2O_5 and $V_2O_{5(1-x)}MoS_{2(x)}$ (X = 1–5% w/w) nanocomposites. The values of (IDF) ε'' were increased as laser-irradiated V_2O_5 while they reduced as $V_2O_{5(1-x)}MoS_{2(x)}$ (X = 1–5% w/w) nanocomposites at 5% of MoS_2 with irradiation of 5 min. The decline in crystalline sizes created the interface area of laser-irradiated V_2O_5 and $V_2O_{5(1-x)}MoS_{2(x)}$ (X = 1–5% w/w) nanocomposites which caused the IP reduced and hence the ε'' improved. An external power supply source

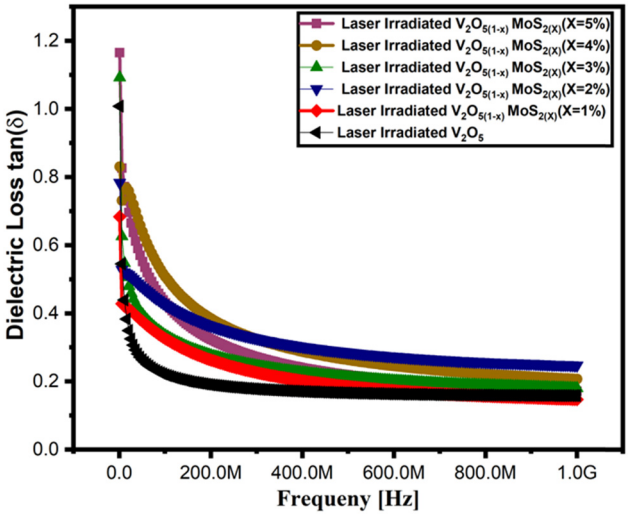

Figure 12: Tangent loss of laser irradiated of $V_2O_{5(1-x)}MoS_{2(x)}$ (X = 1–5% w/w) nanocomposites.

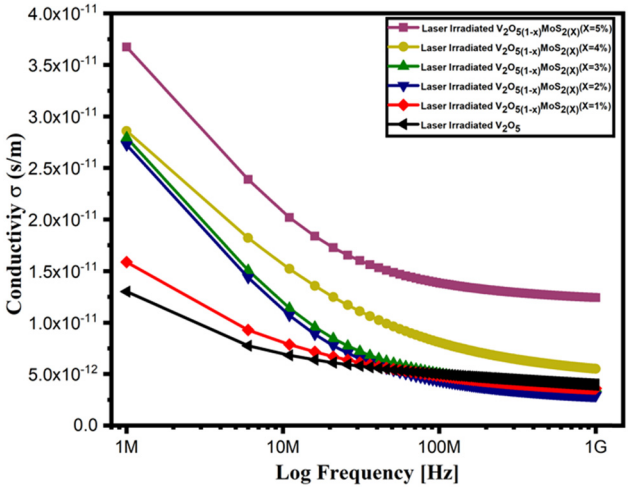

Figure 13: Electric conductivity of laser irradiated of $V_2O_{5(1-x)}MoS_{2(x)}$ (X = 1–5% w/w) nanocomposites.

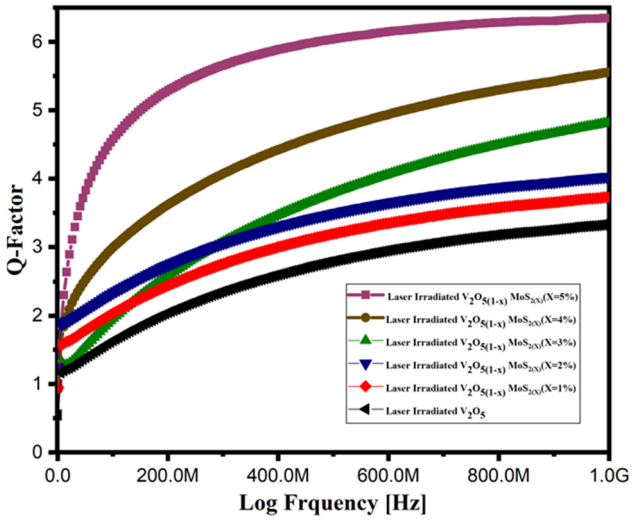

Figure 14: Quality factor of laser irradiated of $V_2O_{5(1-x)}MoS_{2(x)}$ (X = 1–5% w/w) nanocomposites.

connected to a parallel plate capacitor results in a phase angle of 90° between the current and voltage, which leads to current leakage and power dissipation. Thus, the following formula can be used to calculate the tangent loss [32]:

$$\tan\delta = \frac{1}{2\pi f C_p R_p}, \tag{6}$$

where tan δ represents the loss tangent or dielectric loss, C_p is the parallel capacitance, R_p is the parallel resistance, and $2\pi f$ is the angular frequency. Zero loss angle and zero power consumption characterize the perfect capacitor. Power dissipations, often called dielectric loss in commercial capacitors, would be assessed. The variation in dielectric loss (tan δ) as a function of frequency (f) for laser-irradiated pellets that produced pure V_2O_5 and MoS_2-doped-V_2O_5 nanocomposites with varying MoS_2 doping is shown in Figure 12. According to Koop's Phenomenological Theory, these patterns are consistent with the Maxwell–Wagner interface polarization model. The smooth grain is more active at high frequencies, whereas the grain boundary with insufficient conductivity is more efficient in the low-frequency range due to internal morphological defects. Figure 3 illustrates the relaxation peaks for various components that appear at various frequencies. Each polarization mechanism has a unique relaxation frequency, and polarization resonance states that

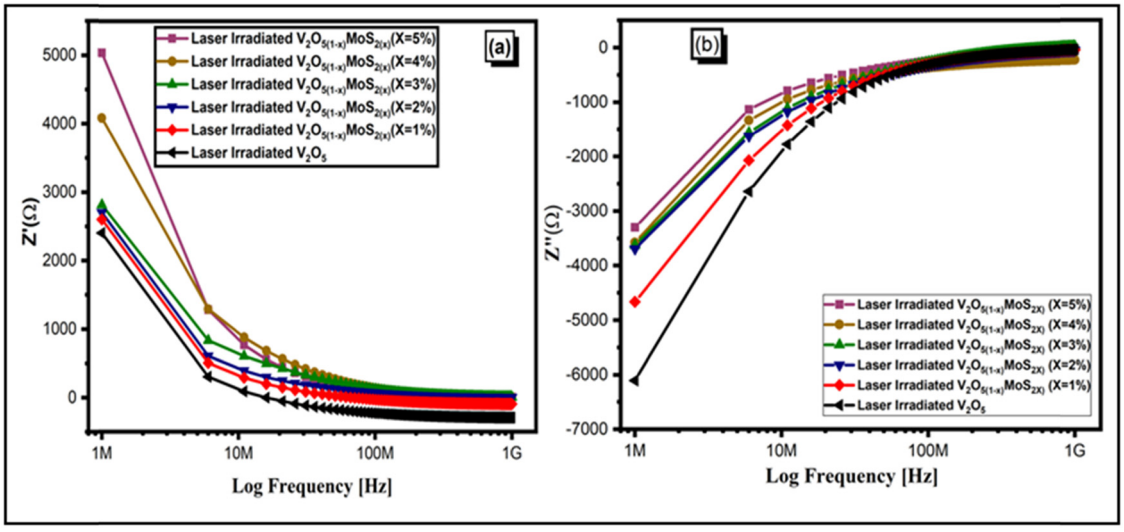

Figure 15: (a, b) Impedance analysis of laser irradiation into $V_2O_{5(1-x)}MoS_{2(x)}$ (X = 1–5% w/w) nanocomposite.

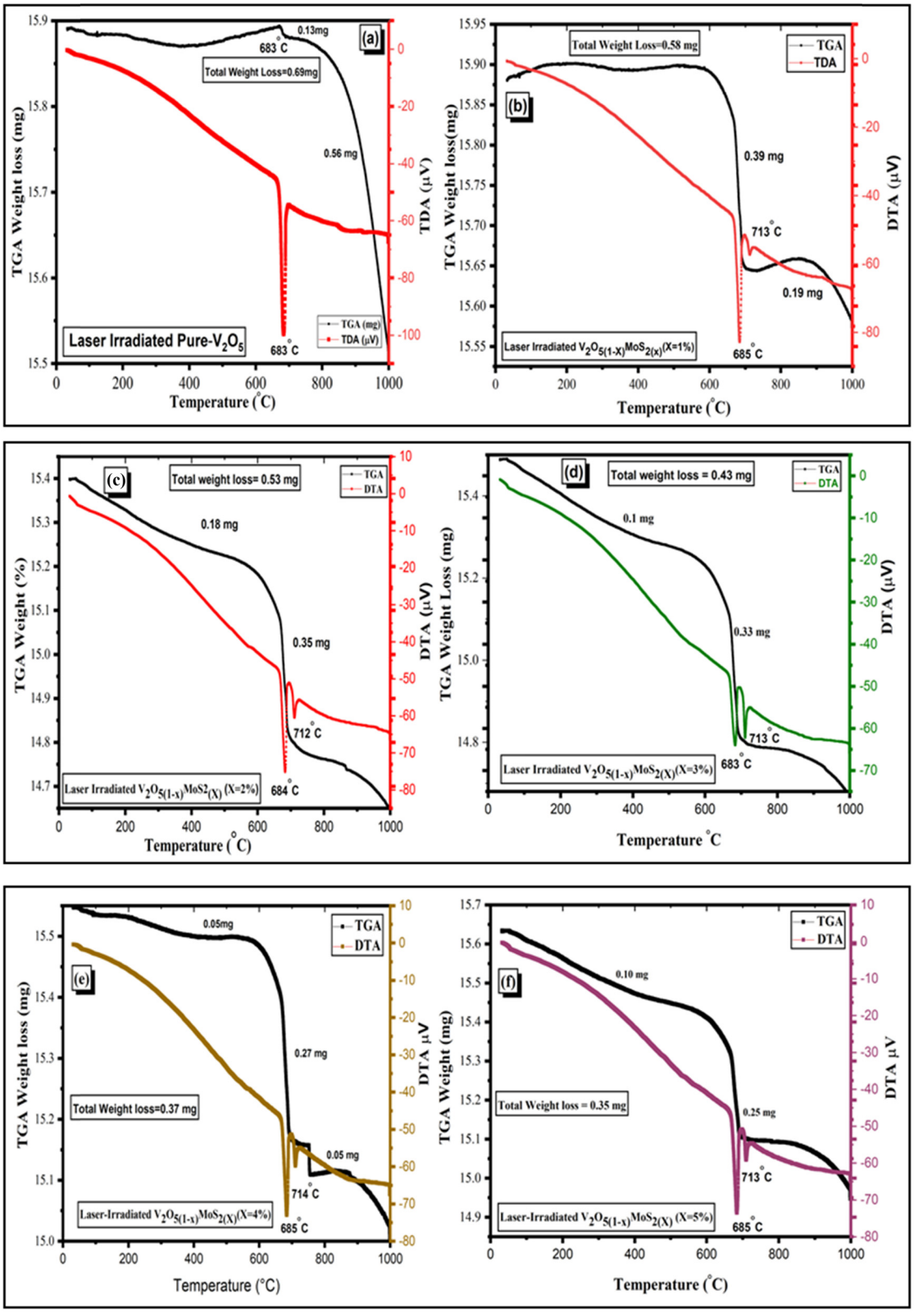

Figure 16: (a–f) Thermal gravimetric and differential thermal analysis of laser irradiated of $V_2O_{5(1-x)}MoS_{2(x)}$ (X = 1–5% w/w) nanocomposites.

Table 5: Thermal stability and weight loss parameters of laser irradiated of $V_2O_{5(1-x)}MoS_{2(x)}$ (X = 1–5% w/w) nanocomposites

Material	First exothermic peak 1st total weight loss (mg)	Second exothermic peak 2nd total weight loss (mg)	Total weight loss (mg)	Temperature (°C)
Laser-irradiated pure-V_2O_5	0.13	0.56	0.69	683
Laser-irradiated $V_2O_{5(1-x)}MoS_{2(x)}$ (X = 1% w/w)	0.39	0.19	0.58	677 713
Laser-irradiated $V_2O_{5(1-x)}MoS_{2(x)}$ (X = 2% w/w)	0.18	0.35	0.53	678 712
Laser-irradiated $V_2O_{5(1-x)}MoS_{2(x)}$ (X = 3% w/w)	0.1	0.33	0.43	673 713
Laser-irradiated $V_2O_{5(1-x)}MoS_{2(x)}$ (X = 4% w/w)	0.1	0.27	0.37	679 714
Laser-irradiated $V_2O_{5(1-x)}MoS_{2(x)}$ (X = 5% w/w)	0.10	0.25	0.35	677 713

resonance occurs when the relaxation frequency and applied frequency are matched. Therefore, the relaxation phenomena of studied samples are responsible for the existence of different component peaks. The relaxation peak changes toward low frequency when the content of MoS_2 increases, suggesting that the relaxation duration may increase. These findings of RDF (ε') and IDF (ε'') and tangent loss of laser-irradiated pure V_2O_5 and MoS_2-doped-V_2O_5 nanocomposites are appropriate for photocatalytic activity.

3.9.2 Conductivity analysis

The movement of a charge carrier in response to an applied field is known as conductivity. At lower 1 MHz frequency, conductivity is at high 1.25×10^{-11} S m^{-1} for pure V_2O_5 and 3.6×10^{-11} S m^{-1} for $V_2O_{5(1-x)}MoS_{2(x)}$ (X = 1–5% w/w) nanocomposite for 5% doping percentage. However, conductivity gradually decreases at higher frequencies as shown in Figure 13. A small conductivity is found at higher frequencies due to the complex resistive nature of grain boundaries. Jonsher's Power Law can be used to determine the net conductivity of ceramic materials [33,34].

$$\sigma_{\text{total}} = \sigma_{\text{dc}} - A\omega^s, \tag{7}$$

where s is the exponent, A is the pre-exponential factor, and σ_{dc} is the DC conductivity. The entire design of $A\omega^s$ is included in the term "ac conductivity." The ac conductivity may be computed using the following formula [35]:

$$\sigma_{\text{ac}} = \varepsilon'\varepsilon_0\omega \tan\delta. \tag{8}$$

Here, angular frequency is represented by ($\omega = 2\pi f$). Figure 4 displays a variation of conductivity (σ_{ac}) *versus* frequency (f) for laser-irradiated pure V_2O_5 and $V_2O_{5(1-x)}MoS_{2(x)}$ (X = 1–5% w/w) nanocomposites with different doping concentration of MoS_2. The change in ac conductivity is large at first, but as the frequency increases, the conductivity decreases gradually with an increment of doping concentration of MoS_2.

3.9.3 Quality factors

The Q factor fluctuation with frequency (f) for laser-irradiated pure V_2O_5 and $V_2O_{5(1-x)}MoS_{2(x)}$ (X = 1–5% w/w) nanocomposites with varying MoS_2 doping concentrations is displayed in Figure 14. The dielectric properties of samples of nanocomposites were studied at a frequency of 1 GHz. The Q factor of laser-irradiated pure V_2O_5 and MoS_2-doped

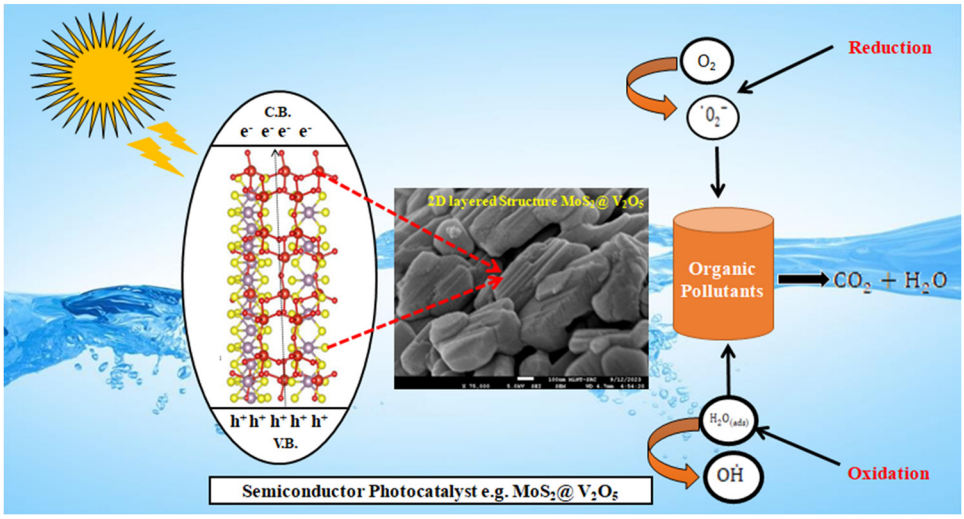

Figure 17: The photocatalytic mechanism of laser irradiated V_2O_5/MoS_2 nanocomposites.

V_2O_5 nanocomposites at higher frequency increases with increasing MoS_2 doping weight percentage.

3.9.4 Complex impedance analysis

An effective method for investigation of the function of grains and grain boundaries as well as the polarization process is impedance spectroscopy. A material's dielectric response is mostly dependent on the resistance and capacitance values of its microstructures, which affect certain solid characteristics. This method enables determining the relaxation time and frequency as well as the resistance and capacitance provided by the bulk and grain boundaries. In complex form, the frequency dependency of impedance may be expressed as [36,37]

$$Z^* = Z' + \quad JZ'', \tag{9}$$

$$\tan\delta = \frac{\varepsilon''}{\varepsilon'} = \frac{Z'}{Z''}, \tag{10}$$

$$Z^* = \frac{\varepsilon''}{C_o\omega(\varepsilon'^2 + \varepsilon''^2)} + j\frac{\varepsilon''}{C_o\omega(\varepsilon'^2 + \varepsilon''^2)}. \tag{11}$$

Figure 15 demonstrates the frequency dependence of real impedance, which shows a diminishing trend as frequency increases. Real impedance's frequency dependency is seen in Figure 15, where an increasing frequency is accompanied by a decreasing trend.

As the frequency increases, the impact of conductive grains causes it to decrease. According to the investigation, as frequency and MoS_2 doping percentage increase, Z' magnitude decrement, suggesting that the sample's conductivity (σ_{dc}) increases. Real impedance Z' gradually drops at low frequencies as MoS_2 substitution increases. Furthermore, it is shown that the MoS_2 concentration increases at low frequencies at which the real impedance Z' peaks meet. Conversely, Figure 15 shows that imaginary impedance Z'' at a higher value with the increment of the frequency with MoS_2 doping concentration.

3.10 Thermogravimetric analysis (TGA) and differential thermal analysis (DTA)

TGA and DTA are efficient studies to understand materials' thermal stability and relative weight loss, respectively. TGA is a quantitative and qualitative investigation of mass to temperature or time as a function. Figure 16(a–f) shows TGA thermograms of pure V_2O_5 and 2D heterostructured layered $V_2O_{5(1-x)}MoS_{2(x)}$ (X = 1–5% w/w) nanocomposites. Thermal investigation revealed a three-phase loss in weight. The first loss in weight below 685°C can be attributed to the removal of physisorbed water molecules and other ions found in pure V_2O_5 and $V_2O_{5(1-x)}MoS_{2(x)}$ (X = 1–5% w/w) nanocomposites. The second thermal degradation occurs in between 687 and 710°C temperature range as a result of the elimination of other ions and the dehydroxylation of metal hydroxide. The oxidation and loss cause the third thermal deterioration, which occurs between 712 and 1,000°C. The weight loss was decreased from 0.69 to 0.35 mg, and thermal stability increased with the increased doping percentage in $V_2O_{5(1-x)}MoS_{2(x)}$ (X = 1–5%w/w) nanocomposites, as shown in Table 5. According to these findings, the pure V_2O_5 and $V_2O_{5(1-x)}MoS_{2(x)}$ (X = 1–5% w/w) nanocomposites were created stable at high temperatures.

Figure 16(a–f) depicts the results of the DTA of pure V_2O_5 and $V_2O_{5(1-x)}MoS_{2(x)}$ (X = 1–5% w/w), which demonstrate the existence of one minor exothermic peak at 710°C and two endothermic peaks at 677 and 712°C. The following equation are related oxidation and decomposition [38]:

$$[V^{4+}] \xrightarrow[\text{Oxidation}]{400-700^{\circ}C} [V^{5+}], \tag{12}$$

$$[MoS_2] \xrightarrow[\text{Oxidation}]{200-500^{\circ}C} [MoO_2] \xrightarrow[\text{decomposition}]{500-1{,}000^{\circ}C} [Mo_2O_2]. \tag{13}$$

3.11 Mechanism of the photocatalytic reaction

The generation of electrons (e^-) and hole (h^+) pairs on the photocatalyst's surface and their transformation to the active sites are produced by the fundamental mechanism of the photocatalytic reaction. The hole (h^+) in the valance band (VB) and electron (e^-) in the conduction band (CB) when exposed to photons of UV light equal to or greater than E_g. This can only be accomplished by having electrons from the VB transfer into the CB. The electron (e^-) in the CB convert oxygen into superoxide ions ($\dot{O}_2^-$), whereas water (H_2O) in the organic dyes MB oxidizes to hydroxyl free radicals ($^-$OH) due to the positively charged hole in the valance band. The oxidation of MB and the reduction of oxygen do not occur at the same time throughout the remediation process, as presented in Figure 17. Recombination of electrons (e^-) and positive hole (h^+) is caused by the concentration of (e^-) in the CB The electrons are necessary for the photocatalytic redox reactions to produce superoxide ions ($\dot{O}_2^-$), and hydroxyl free radicals (−OH). As during this degradation process organic dye molecules split into CO_2 and H_2O, and produced more −OH and $\dot{O}_2^-$ due to newly generated active sites as powerful oxidizers with increase of MoS_2 dopants in nanocomposites. Consequently, MB remediation increases at a faster rate. The photocatalytic mechanism's schematic depiction may be explained by applying formulae to determine the energies of MoS_2 and V_2O_5 VB and CB [39]

$$E_{VB} = \chi - E_e + (0.5), \tag{14}$$

$$E_{CB} = E_{VB} - E_g. \tag{15}$$

Free electron energy on the hydrogen scale, band gap, CB, and VB edges are represented, respectively, by variables E_e, E_g, E_{CB}, andE_{VB}. Additionally, χ represents the electro-negativity of the material.

The possible mechanism of photocatalysts (MoS_2-doped-V_2O_5) with p–n heterojunction subjected to sunlight. Photogenerated carriers are kept apart in the p–n heterojunction by the n-type MoS_2 and the p-type V_2O_5. A depletion zone with positively and negatively charged regions in the V_2O_5 and MoS_2 sides, correspondingly, is created at the heterojunction when n-type and p-type nanocomposites are linked because of their Fermi levels aligning. When sunshine photons are exposed to a semiconductor, photogenerated (e^-) are moved from the V_2O_5 VB to the MoS_2-doped-V_2O_5 CB. The superoxide radical ($\dot{O}_2^-$) is created when these electrons join with the oxygen molecules in the dissolved solution. This radical then changes into the highly reactive hydroxide radicals (−OH). Nevertheless, hole transfer from the valance band of V_2O_5 to MoS_2-doped-V_2O_5 was impeded by the high potential barrier. The H_2O molecules oxidize into hydroxyl radicals (−OH) due to the holes in the nanocomposites. Strong oxidizing radicals like these readily oxidize the chemical molecules in MB. Compared to metal oxide equivalents, MoS_2-doped-V_2O_5 nanocomposites show superior photocatalytic activity because of their enhanced efficiency of photogenerated charge carrier separation. Based on the above experimental results, a possible process for the photocatalytic degradation of MB *via* MoS_2-doped-V_2O_5 is proposed in equations (16)–(20) [40].

$$\begin{aligned} &MoS_2\text{-doped-}V_2O_5 + h\nu(\text{visible light}) \\ &\rightarrow MoS_2 \quad (h^+, e^-) + V_2O_5 \quad (h^+, e^-), \end{aligned} \tag{16}$$

$$MoS_2(h^+, e^-) + V_2O_5(h^+, e^-) \rightarrow V_2O_5(h^+) + MoS_2(e^-), \tag{17}$$

$$e^- + O_2 \rightarrow \dot{O}_2^-, \tag{18}$$

$$h^+ + H_2O \rightarrow -OH, \tag{19}$$

$$\begin{aligned} &-OH + \dot{O}_2^- + \text{Methylene Blue} \rightarrow \text{intermediates} \\ &\rightarrow CO_2 + H_2O. \end{aligned} \tag{20}$$

In the MoS_2-doped-V_2O_5 nanocomposites, the photogenerated charge carriers increase because of the low recombination rate as a consequence of injecting charge carriers from materials with high band gaps toward the small band gaps. These results demonstrate that the photocatalytic activity is boosted due to MoS_2-doped-V_2O_5 nanocomposites on MB degradation compared to other separated single materials such as MoS_2 and V_2O_5.

4 Conclusion

It has been discovered that both 2D MoS_2 and V_2O_5, which are classified as TMDs and TMOs, are good photocatalyst materials. The surface of the 2D molybdenum nanolayered matrix was efficaciously decorated with V_2O_5 NPs. In the range of the UV visible spectrum, the increment in optical conductivity from 3.6 to 14.5 $\Omega^{-1}\,cm^{-1}$ with an increase of the active surface from 108 to 169 μm^2. The synthesized

nanocomposites show an increase in absorbance from 3 to 8.3 a.u. at wavelength 310 nm. According to PL studies, the intensity of peaks decreases when laser irradiation time and doping percentages are increased. As a result, a small peak indicates a decrement rate of electron-hole pair recombination, which increases the capacity for separation.TGA and DTA results revealed that weight loss decreased from 0.69 to 0.35 mg and thermal stability increased with increased doping concentrations. MB was degraded in 150 min, proving that the prepared MoS_2-doped-V_2O_5 material was a stable and economically low-cost nanocomposite for photocatalytic activity.

Acknowledgments: The authors extend their appreciation to Taif University, Saudi Arabia, for supporting this work through project number (TU-DSPP-2024-59).

Funding information: This research was funded by Taif University, Saudi Arabia, Project No. (TU-DSPP-2024-59).

Authors contributions: Muhammad Hasnain Jameel: writing – original draft, data curation, experimental work, visualization, writing – review and editing, investigation, formal analysis, methodology, validation; Aqeela Yasin: review and editing, Samia: review and editing; Mohd Zul Hilmi Bin Mayzan: supervision, review and editing; Muhammad Sufi bin Roslan: review and editing, Fahmiruddin Bin Esa: review and editing, Mohd Arif Bin Agam: Supervision, Review & editing. Khaled Althubeiti: review and editing, Mohammed Aljohani: review and editing. All authors have accepted responsibility for the entire content of this manuscript and approved its submission.

Conflict of interest: The authors state no conflict of interest.

Data availability statement: The datasets generated and/or analysed during the current study are available from the corresponding author on reasonable request.

References

[1] Navyashree GR, Hareesh K, Sunitha DV, Nagabhushana H, Nagaraju G. Photocatalytic degradation performance of Nd3 + doped V2O5 nanostructures. Mater Res Express. 2018;5(9):095007. doi: 10.1088/2053-1591/aad373.

[2] Tan D, Long H, Zhou H, Deng Y, Liu E, Wang S, et al. Effective photocatalytic degradation of methyl orange using V2O5@ZnO nanocomposite under UV and visible irradiations. Int J Electrochem Sci. 2020;15:12232–43. doi: 10.20964/2020.12.75.

[3] Jayaraman V, Sarkar D, Rajendran R, Palanivel B, Ayappan C, Chellamuthu M, et al. Synergistic effect of band edge potentials on BiFeO3/V2O5 composite: Enhanced photo catalytic activity. J Environ Manage. 2019;247:104–14. doi: 10.1016/j.jenvman.2019.06.041.

[4] Rafique M, Hamza M, Tahir MB, Muhammad S, Al-Sehemi AG. Facile hydrothermal synthesis of highly efficient and visible light-driven Ni-doped V2O5 photocatalyst for degradation of Rhodamine B dye. J Mater Sci Mater Electron. 2020;31(15):12913–25. doi: 10.1007/s10854-020-03844-3.

[5] Jayaraj SK, Sadishkumar V, Arun T, Thangadurai P. Enhanced photocatalytic activity of V2O5 nanorods for the photodegradation of organic dyes: A detailed understanding of the mechanism and their antibacterial activity. Mater Sci Semicond Process. 2018;85:122–33. doi: 10.1016/j.mssp.2018.06.006.

[6] Zeleke MA, Kuo DH. Synthesis and application of V2O5-CeO2 nanocomposite catalyst for enhanced degradation of methylene blue under visible light illumination. Chemosphere. 2019;235:935–44. doi: 10.1016/j.chemosphere.2019.06.230.

[7] Zhang S, Chen S, Luo Y, Yan B, Gu Y, Yang F, et al. Large-scale preparation of solution-processable one-dimensional V2O5 nanobelts with ultrahigh aspect ratio for bifunctional multicolor electrochromic and supercapacitor applications. J Alloys Compd. 2020;842:155882. doi: 10.1016/j.jallcom.2020.155882.

[8] Menezes WG, Reis DM, Benedetti TM, Oliveira MM, Soares JF, Torresi RM, et al. V2O5 nanoparticles obtained from a synthetic bariandite-like vanadium oxide: Synthesis, characterization and electrochemical behavior in an ionic liquid. J Colloid Interface Sci. 2009;337(2):586–93. doi: 10.1016/j.jcis.2009.05.050.

[9] Zhou F, Yan C, Sun Q, Komarneni S. TiO2/Sepiolite nanocomposites doped with rare earth ions: Preparation, characterization and visible light photocatalytic activity. Microporous Mesoporous Mater. 2019;274:25–32. doi: 10.1016/j.micromeso.2018.07.031.

[10] Zia J, Kashyap J, Riaz U. Facile synthesis of polypyrrole encapsulated V2O5 nanohybrids for visible light driven green sonophotocatalytic degradation of antibiotics. J Mol Liq. 2018;272:834–50. doi: 10.1016/j.molliq.2018.10.091.

[11] Jayaraj SK, Thangadurai P. Surface decorated V2O5 nanorods with Pt nanoparticles for enriched visible light photocatalytic performance for the photodegradation of Rh-6G. J Mol Liq. 2020;319:114368. doi: 10.1016/j.molliq.2020.114368.

[12] Pooseekheaw P, Thongpan W, Panthawan A, Kantarak E, Sroila W, Singjai P. Porous V2O5/TiO2nanoheterostructure films with enhanced visible-light photocatalytic performance prepared by the sparking method. Molecules. 2020;25(15):1–11. doi: 10.3390/molecules25153327.

[13] Zhang X, Teng SY, Loy ACM, How BS, Leong WD, Tao X. Transition metal dichalcogenides for the application of pollution reduction: A review. Nanomaterials. 2020;10(6):1012. doi: 10.3390/nano10061012.

[14] Gao XT, Liu YT, Zhu XD, Yan DJ, Wang C, Feng YJ, et al. V2O5 nanoparticles confined in Three−Dimensionally organized, porous Nitrogen−Doped graphene frameworks: Flexible and Free −Standing cathodes for high performance lithium storage. Carbon N Y. 2018;140:218–26. doi: 10.1016/j.carbon.2018.08.060.

[15] Mishra A, Panigrahi A, Mal P, Penta S, Padmaja G, Bera G, et al. Rapid photodegradation of methylene blue dye by rGO- V2O5 nano composite. J Alloys Compd. 2020;842:155746. doi: 10.1016/j.jallcom.2020.155746.

[16] Yuan Y, Guo Rt, Hong Lf, Ji Xy, Li Zs, Lin Zd, et al. Recent advances and perspectives of MoS2-based materials for photocatalytic dyes degradation: A review. Colloids Surf A Physicochem Eng Asp. 2021;611:125836. doi: 10.1016/j.colsurfa.2020.125836.

[17] Huang S, Chen C, Tsai H, Shaya J, Lu C. Photocatalytic degradation of thiobencarb by a visible light-driven MoS2 photocatalyst. Sep Purif Technol. 2018;197(2017):147–55. doi: 10.1016/j.seppur.2018.01.009.
[18] Wu MH, Li L, Liu N, Wang DJ, Xue YC, Tang L. Molybdenum disulfide (MoS2) as a co-catalyst for photocatalytic degradation of organic contaminants: A review. Process Saf Environ Prot. 2018;118:40–58. doi: 10.1016/j.psep.2018.06.025.
[19] Hunge YM, Yadav AA, Kang SW, Jun Lim S, Kim H. Visible light activated MoS2/ZnO composites for photocatalytic degradation of ciprofloxacin antibiotic and hydrogen production. J Photochem Photobiol A Chem. 2023;434(2022):114250. doi: 10.1016/j.jphotochem.2022.114250.
[20] Khaing KK, Yin D, Ouyang Y, Xiao S, Liu B, Deng L, et al. Fabrication of 2D-2D heterojunction catalyst with covalent organic framework (COF) and MoS2 for highly efficient photocatalytic degradation of organic pollutants. Inorg Chem. 2020;59(10):6942–52. doi: 10.1021/acs.inorgchem.0c00422.
[21] Ahamad T, Naushad M, Al-Saeedi SI, Almotairi S, Alshehri SM. Fabrication of MoS2/ZnS embedded in N/S doped carbon for the photocatalytic degradation of pesticide. Mater Lett. 2020;263:127271. doi: 10.1016/j.matlet.2019.127271.
[22] Cao X, Gan X, Lang H, Peng Y. Impact of the surface and microstructure on the lubricative properties of MoS2 aging under different environments. Langmuir. 2021;37(9):2928–41. doi: 10.1021/acs.langmuir.0c03512.
[23] Lu D, Yang M, Wang H, Kiran Kumar K, Wu P, Neena D. In situ hydrothermal synthesis of Y-TiO2/graphene heterojunctions with improved visible-light-driven photocatalytic properties. Ceram Int. 2017;43(18):16753–62. doi: 10.1016/j.ceramint.2017.09.070.
[24] Asaithambi S, Sakthivel P, Karuppaiah M, Balamurugan K, Yuvakkumar R, Thambidurai M, et al. Synthesis and characterization of various transition metals doped SnO2@MoS2 composites for supercapacitor and photocatalytic applications. J Alloys Compd. 2021;853:157060. doi: 10.1016/j.jallcom.2020.157060.
[25] Krishnan U, Kaur M, Kaur G, Singh K, Dogra AR, Kumar M, et al. MoS2/ZnO nanocomposites for efficient photocatalytic degradation of industrial pollutants. Mater Res Bull. 2019;111:212–21. doi: 10.1016/j.materresbull.2018.11.029.
[26] Li L, Yin X, Sun Y. Facile synthesized low-cost MoS2/CdS nanodots-on-nanorods heterostructures for highly efficient pollution degradation under visible-light irradiation. Sep Purif Technol. 2019;212:135–41. doi: 10.1016/j.seppur.2018.11.032.
[27] Ramsha K, Adeel R, Sofia J, Rahim J, Muhammad AA, Mohammad M. Synthesis and characterization of MoS2/TiO2 nanocomposites for enhanced photocatalytic degradation of methylene blue under sunlight irradiation. Key Eng Mater. 2018;778:137–43. doi: 10.4028/www.scientific.net/KEM.778.137.
[28] Wu D, Han L. Solvothermal synthesis and characterization of visible-light-active MoO3/MoS2 heterostructure. J Sol-Gel Sci Technol. 2019;91(3):441–5. doi: 10.1007/s10971-019-05056-6.
[29] Xavier JR. High protection performance of vanadium pentoxide-embedded polyfuran/epoxy coatings on mild steel. Polym Bull. 2021;78(10):5713–39. doi: 10.1007/s00289-020-03400-3.
[30] Wang Y, Li J, Wei Z. Transition-metal-oxide-based catalysts for the oxygen reduction reaction. J Mater Chem A. 2018;6(18):8194–209. doi: 10.1039/c8ta01321g.
[31] Gao MR, Liang JX, Zheng YR, Xu YF, Jiang J, Gao Q, et al. An efficient molybdenum disulfide/cobalt diselenide hybrid catalyst for electrochemical hydrogen generation. Nat Commun. 2015;6:1–7. doi: 10.1038/ncomms6982.
[32] Hasnain M, Muhammad J, Mohd R, Bin A. Effect of external static pressure on structural, electronic, and optical properties of 2 - D hetero - junction MoS 2 for a photocatalytic applications: A DFT study. Opt Quantum Electron. 2023;2:1–14. doi: 10.1007/s11082-023-04853-2.
[33] Shafeeq KM, Athira VP, Kishor CHR, Aneesh PM. Structural and optical properties of V2O5 nanostructures grown by thermal decomposition technique. Appl Phys A Mater Sci Process. 2020;126(8):586. doi: 10.1007/s00339-020-03770-5.
[34] Jameel MH, Roslan M, Mayzan M, Shaaban IA, Rizvi S, Agam M, et al. A comparative DFT study of bandgap engineering and tuning of structural, electronic, and optical properties of 2D WS2, PtS2, and MoS2 between WSe2, PtSe2, and MoSe2 materials for photocatalytic and solar cell applications. J Inorg Organomet Polym Mater. 2023;34:322–35. doi: 10.1007/s10904-023-02828-0.
[35] Shaaban ER, Hassaan MY, Mostafa AG, Abdel-Ghany AM. Crystallization kinetics of new compound of V2O5-PbO-Li2O-Fe2O3 glass using differential thermal analysis. J Alloys Compd. 2009;482(1–2):440–6. doi: 10.1016/j.jallcom.2009.04.062.
[36] Jameel MH, Bin Agam MA, bin Roslan MS, Jabbar AH, Malik RQ, Islam MU, et al. A comparative DFT study of electronic and optical properties of Pb/Cd-doped LaVO4 and Pb/Cd-LuVO4 for electronic device applications. Comput Condens Matter. 2023;34(2022):e00773. doi: 10.1016/j.cocom.2022.e00773.
[37] Grandgirard J, Poinsot D, Krespi L, Nénon JP, Cortesero AM. Costs of secondary parasitism in the facultative hyperparasitoid Pachycrepoideus dubius: Does host size matter? Entomol Exp Appl. 2002;103(3):239–48. doi: 10.1023/A:1021193329749.
[38] Jameel MH, Ahmed S, Jiang ZY, Tahir MB, Akhtar MH, Saleem S, et al. First principal calculations to investigate structural, electronic, optical, and magnetic properties of Fe3O4and Cd-doped Fe2O4. Comput Condens Matter. 2022;30(2021):e00629. doi: 10.1016/j.cocom.2021.e00629.
[39] Joiner RL, Vinson SB, Benskin JB. Teratocytes as a source of juvenile hormone activity in a parasitoid-host relationship. Nat New Biol. 1973;246(152):120–1. doi: 10.1038/newbio246120a0.
[40] Jameel MH, Rehman A, bin Roslan MS, Bin Agam MA. To investigate the structural, electronic, optical and magnetic properties of Sr-doped KNbO3 for perovskite solar cell applications: A DFT study. Phys Scr. 2023;98(5):055802. doi: 10.1088/1402-4896/acc6fb.